



Research Paper

Parameter optimisation of a centrifugal fan for rice combine harvesters based on airflow resistance coefficients and CFD simulations

Zhenwei Liang ^a , Million Eyaus Wada ^{a,b,*} ^a School of Agricultural Engineering, Jiangsu University, Zhenjiang, 212013, China^b Department of Agricultural Engineering, Haramaya Institute of Technology, Haramaya University, P.O. Box 138, Dire Dawa, Ethiopia

ARTICLE INFO

ABSTRACT

Keywords:

Cleaning fan
Feed rate
Airflow resistances
Airflow velocity
Optimisation

In this work, both experimental and numerical simulations were employed to identify optimal fan parameter settings for achieving efficient cleaning performance during high-yield rice harvesting. First, field experiments were conducted to analyse the distribution of threshed outputs within the cleaning shoe, and then airflow resistance coefficients created by the fluidised grain and cleaning sieves in each zone were calculated. Subsequently, perforated plates were designed based on the calculated airflow resistance coefficients in different sieve zones to represent the cleaning load. The computational fluid dynamics (CFD) simulation results were validated by using measured airflow velocity at multiple points beneath the perforated plates. After validation, additional CFD simulations were performed under various fan parameter settings, incorporating porous media to simulate the fan's working load. The results indicated that a sieve opening of 26 mm, guide plate angles (I) of 38° and (II) of 36°, and a fan speed of 1300 rpm significantly improved airflow and pressure distribution within the fan. Finally, a field experiment validated the cleaning performance using the selected parameter combinations, achieving a grain sieve loss ratio of 0.78 % and a grain impurity ratio of 1.15 % at a feed rate of 6 kg s⁻¹. This innovative approach not only provides an accurate method for determining the fan's working load but also enables the evaluation of fan performance under varying load conditions through CFD simulations, ultimately enhancing the cleaning performance of rice combine harvesters through optimised parameter selection.

Nomenclature

(continued)

| | | | |
|-----------------|---|------------|--|
| A ₀ | Sieve opening area, m ² | α | Permeability of porous media, m ² |
| A ₁ | Coefficient for viscous component | β | Open area of perforated plate, % |
| A _t | Maximum sieve opening area, m ² | ϵ | Rate of dissipation of turbulent |
| A _z | Area of sieve section, m ² | e_f | Porosity of a fluidised grain, % |
| B ₁ | Coefficient for inertial component | λ | Sieve opening ratio, % |
| C ₂ | Inertial resistance, m ⁻¹ | μ | Viscosity of air, N (m s) ⁻¹ |
| c _f | Total resistance coefficient | ρ_a | Airflow density, 1.225 kg m ⁻³ |
| c _{fz} | Resistance due to the grain | δ | Thickness of porous media, mm |
| c _{ls} | Resistance due to the lower sieve | ρ_g | Density of grain, 1350 kg m ⁻³ |
| c _{us} | Resistance due to the upper sieve | ΔP | Pressure drop, Pa |
| g | Gravitational acceleration, m s ⁻² | Δt | Time step size, s |
| G _l | Grain sieve loss ratio, % | BBB | Box–Behnken Design |

(continued on next column)

| H _f | Height of fluidised grain, m | CFD | Computational Fluid Dynamics |
|-----------------|--|------------------|---|
| I _m | Grain impurity ratio, % | DOE | Design of Experiment |
| k | Turbulent kinetic energy | FOD | First-Order Discretisation |
| M _f | Mass of fluidised grain, kg | HWA | Hotwire Anemometer |
| Q | Airflow flow rate, m ³ s ⁻¹ | ICEM | Integrated Computer Engineering and Manufacturing |
| q | Dynamic pressure, Pa | MOG | Material Other than Grain |
| R | Fan revolution speed, rpm | MOG _T | MOG mass in grain sample, g |
| V _{1o} | Fan outlet velocity, m s ⁻¹ | MRF | Multiple Reference Frame |
| V _{f1} | Fluidisation velocity at front, m s ⁻¹ | | |
| V _{f2} | Fluidisation velocity at middle, m s ⁻¹ | RHS | Right Hand Side |
| V _{f3} | Fluidisation velocity at rear, m s ⁻¹ | RMSE | Root Mean Square Error |
| w _g | Grain mass in the perforated bag, g | RNG | Re-Normalisation Group |
| w | Grain mass in grain tank, g | RSM | Response Surface Methodology |

(continued on next page)

* Corresponding author. School of Agricultural Engineering, Jiangsu University, Zhenjiang, 212013, China.

E-mail addresses: zhenwei_liang@ujs.edu.cn (Z. Liang), millioneyasu9192@gmail.com (M.E. Wada).

(continued)

| | | | |
|-----|---|--------|--|
| Z | Measuring zones on the sieve section, m | SIMPLE | Semi-Implicit Method for Pressure-Linked Equations |
| 1a, | Atmospheric pressure, Pa | | |
| 2a | | | |

1. Introduction

Rice (*Oryza sativa* L.) is a staple food for more than half of the world's population (Chen et al., 2021; Peng et al., 2009), and China is one of the leading rice producers (Nie & Peng, 2017). In recent decades, rising global demand for rice has driven significant advancements in breeding high-yield rice varieties and harvesting technologies, particularly in China (Ji et al., 2022; Liang & Million, 2023; Liu et al., 2022; Qing, Li, Yang, et al., 2021; Qing, Li, Xu, et al., 2021; Wang et al., 2023; Yu et al., 2024). The widespread use of rice combine harvesters, particularly those equipped with a single longitudinal threshing cylinder and a cleaning unit consisting of a centrifugal fan, grain pan, and dual-sieve, has significantly increased rice harvesting efficiency in China (Liang et al., 2016; Liu et al., 2025; Xu et al., 2013; Yuan, 2017). However, increased rice yields have introduced a significant challenge to cleaning performance due to the inherently uneven cleaning loads and uneven airflow distribution inside the cleaning shoe (Ding et al., 2022; Liang et al., 2019; Ma, Zhang, et al., 2023; Zhang et al., 2023). To address these challenges, researchers have focused on improving airflow control within the cleaning shoe. Key research efforts include addressing airflow measurements. Computational Fluid Dynamics (CFD) simulations.

For airflow measurements, Kenney, Wright, and Bryden (2005) employed particle image velocimetry to analyse the internal airflow distribution within a cleaning shoe. Liu et al. (2015) enhanced cleaning efficiency by optimising the arrangement and operating parameters of cleaning components. Xu and Li (2020) examined airflow effects in a threshing and cleaning system by exploring various fan speeds (1200, 1300, 1400, and 1500 rpm), air distributor angles (22°, 24°, 26°, and 28°), and chaffer sieve openings (20, 22, 24, and 26 mm). Liang et al. (2020) identified optimal cleaning performance with a fan speed of 1100 rpm, a sieve opening of 20 mm, and guide plate angles of 8° and 45° by airflow velocity measurement. Ma et al. (2024) investigated the influence of air intake throttling on the fan performance under different diffusion angles (20°, 40°, and 60°), generating performance curves using the measured data and analysing airflow variations at different volume rates.

When combined with experimental data, CFD serves as a powerful tool for simulating, designing, optimising, and analysing flow fields in turbomachinery. Gebrehiwot et al. (2010a) utilised CFD to study the effect of the addition of a cross-flow opening on the performance of the fan, and indicated that the addition of the cross-flow opening across the whole width played an important role for the axial distribution of airflow in the outlets. Christian et al. (2013) numerically studied airflow fields in a cleaning shoe under both loaded and unloaded conditions using CFD. Liang et al. (2020) also applied CFD simulations to study airflow distribution within the cleaning shoe, validating their findings through hot-wire anemometry. Xu and Li (2020) employed CFD simulations to analyse the effects of fan guide plate angles, sieve openings, and threshing cylinder rotational speed on the airflow field within the cleaning shoe.

While previous studies have advanced the understanding of airflow velocity, CFD validation, and experimental techniques, several challenges remain. Many existing systems fail to achieve optimal performance due to inherent design limitations and complex parameter interactions. Furthermore, fan design and development often demand significant time and resources, and field experiments are constrained by seasonal planting cycles (Chu, 2014; Liang et al., 2022; Ma, Zhu, et al., 2023). Extensive studies have been conducted to achieve uniform airflow velocity at the fan outlets and balanced pressure distribution within the fan. However, few studies have directly examined the impact

of cleaning loads on airflow velocity and pressure distribution inside the fan and its outlet. A common method used to simulate the fan's working load involves placing perforated plates at the fan outlets. This method oversimplifies actual conditions by failing to account for variations in airflow resistance among different fan outlets. Fixed combinations of perforated plates may result in non-optimal airflow distributions and deviations in reported results (Gebrehiwot et al., 2010b; Liang et al., 2020). Consequently, accurately determining the fan's working load remains a critical and unresolved challenge in optimising fan performance.

Despite progress in airflow measurement and CFD-based research, accurately determining the working load of a cleaning fan and identifying its optimal operating parameters remain unresolved challenges in rice combine harvesters. This study hypothesises that realistic cleaning load analysis, combined with the optimisation of key fan working parameters (feed rate, guide plate angle, and fan speed), can provide a more reliable basis for determining the fan's working load and improving cleaning performance during rice harvesting. The objective is to address this gap by quantifying the fan's working load and identifying optimal parameter settings through experimental measurements and CFD simulations to enhance airflow distribution and cleaning efficiency. The significance of this study lies in optimising airflow distribution within the cleaning shoe, thereby improving cleaning efficiency in modern rice combine harvesters and ultimately contributing to greater farmer profitability.

2. Materials and methods

2.1. Structure of the cleaning system in the referenced rice combine harvester

The referenced longitudinal-flow crawler-type rice combine harvester (4LZ-6.0 EK, World Group, Zhenjiang, China) with a cutting width of 2200 mm, a threshing cylinder with a diameter of 620 mm, and a longitudinal length of 2010 mm. The cleaning unit consists of a four-bladed centrifugal fan, a grain pan, and a dual-sieve arrangement (adjustable louvers as upper sieve and woven sieve as lower sieve, with overall dimension of the woven sieve of 1500 mm × 1050 mm (length × width) and a mesh size of 22 mm × 22 mm × ϕ 2.5 mm), as shown in Fig. 1(a).

The fan generates the necessary airflow within the cleaning shoe to facilitate the pneumatic separation of grain from material other than grain (MOG), to align the grain over the sieve openings for effective stratification, and to move grain to subsequent sieve holes if they do not initially pass through (Tabatabaifar, 1992). The cleaning fan in this combine harvester is a centrifugal fan, featuring an impeller with four blades, enclosed within and rotating inside a volute, as shown in Fig. 1 (b). Air enters the impeller axially and is discharged at the periphery through three ducts as the impeller rotates within the volute. Optimising the fan's working parameters is crucial to meet the airflow requirements for high-yield rice varieties and to maintain effective cleaning performance.

2.2. Threshed output collection method

The distribution of threshed outputs on the cleaning sieve has a significant effect on the cleaning performance (Li & Li, 2015). Analysing the distribution of threshed output is crucial for understanding the material layer over the sieve surface, for calculating the airflow resistance due to fluidised grain, for identifying areas where the sieve is overloaded, and for determining the working load of the cleaning fan. The experiment to collect threshed output is conducted during the rice harvesting season (2023) in Zhenjiang, Jiangsu Province, China. In this field experiment, the cleaning sieve of the existing longitudinal flow rice combine harvester is removed from its original position, as shown in Fig. 2(a), and replaced by a receiving box. To calculate the airflow

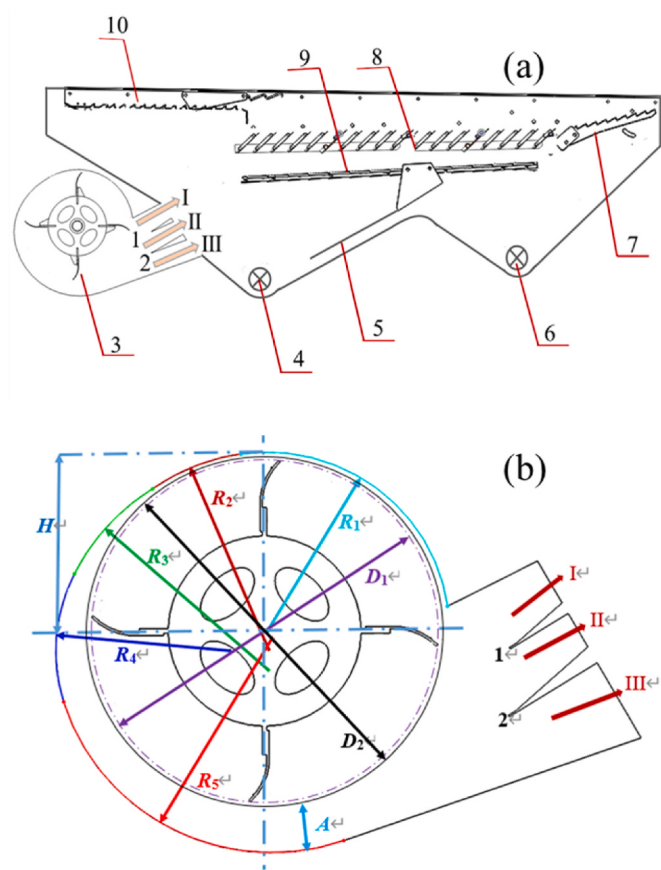


Fig. 1. Schematic diagrams of the referenced cleaning system in the rice combine harvester; (a) Schematic diagram of the referenced cleaning shoe, I – Duct 1, II – Duct 2, III – Duct 3, 1 - guide plate I, 2 - guide plate II, 3 - fan blades, 4 - grain auger, 5 - grain guide plate, 6 - tailings auger, 7 - tailings sieve, 8 - upper sieve, 9 - lower sieve, 10 - grain pan, and (b) Schematic diagram of the referenced cleaning fan, D_1 = impeller inside diameter, 389.65 mm; D_2 = impeller inside diameter, 409.65 mm; R_1 = 211.30 mm; R_2 = 240.48 mm; R_3 = 248 mm; R_4 = 199.03 mm; R_5 = 248.53 mm.

resistance caused by fluidised grain at different locations on the sieve, the receiving box is divided into nine measurement zones (Z_1 to Z_9), as shown in Fig. 2(b). Each grid measures 150 mm in length, width, and depth, the areas A_z , for the nine zones, are 0.135, 0.135, 0.203, 0.180, 0.18, 0.270, 0.135, 0.135, 0.203 m^2 , respectively. These separated zones allow for a detailed analysis of how airflow resistance (c_f) varies across the different sieve areas and to determine the pressure drop (ΔP) along

transverse and longitudinal sieve directions.

The harvested rice crop has an average height of 865 mm and a straw/grain ratio of 2.2, an average one-thousand kernel weight of 30 g, and an average grain yield of 8521 kg ha^{-1} . The average moisture content is 71.1 % and 24.5 % for the straw and grain, respectively. During the experiment, the cleaning fan is kept idle to allow the threshed output to be collected directly from the threshing system. The forward speed of the combine harvester is manually adjusted to achieve feed rates of 5 kg s^{-1} (forward speed 0.8 m s^{-1}), 6 kg s^{-1} (forward speed 1.0 m s^{-1}), and 7 kg s^{-1} (forward speed 1.25 m s^{-1}). After completing the experiment, the receiving box is carefully removed from the cleaning shoe. The components of the threshed output mixture in each zone, including grain and MOG, are then separated and weighed using an electronic scale (RC-JA1003, Shanghai Precision Scientific Instrument Co., Ltd., Shanghai, China) with an accuracy of 0.001 g.

2.3. Airflow resistance (c_f) calculations and perforated plates design

In the referenced combine harvester, a grain mat, mixed layer of the threshed grain, chaff, and other small debris is transferred from the front to the end of the oscillating sieve as most of the rice is threshed in the front part of the threshing cylinder. This layer is supposed to be broken up by airflow from a fan and by mechanical forces when entering the chaffer sieve. The fan blows airflow at an angle through the sieves. When airflow passes through a layer of bulk agricultural material, resistance to the flow referred to as pressure drop develops due to energy losses from friction and turbulence (Brooker, Bakker, & Hall, 1992; Hall, 1980). This resistance, which must be overcome by airflow moving through a packed bed of biological material (e.g., bulk grain), is expressed as the pressure drop per unit bed depth. Based on the superposition principle for a linear system (Qiu, 2006), the resistance distributed across different ducts can be modeled, as schematically shown in Fig. 3, by assuming that the cleaning shoe is filled with the threshed output mixture. Since the clearance of the tailings sieve is approximately 40 mm, the retention time for short straw on the sieve is relatively short, and the material mixture is highly dispersed. Therefore, the resistances from the tailings sieve and the material on it were neglected (Tabatabaifar & Persson, 1995).

2.3.1. Resistance due to fluidised grains

Depending on the airflow velocity, different behaviours of the material layer can occur. At low air velocity, the air moves through the porous material without altering its thickness. As the airflow increases, voids in the material expand due to higher internal forces, causing the layer to expand in height and become fluidised. When the pressure difference across the layer equals the gravitational force of the material, the entire layer is lifted intact. At even higher specific airflow rates, the layer dissolves, and particles no longer support each other, moving

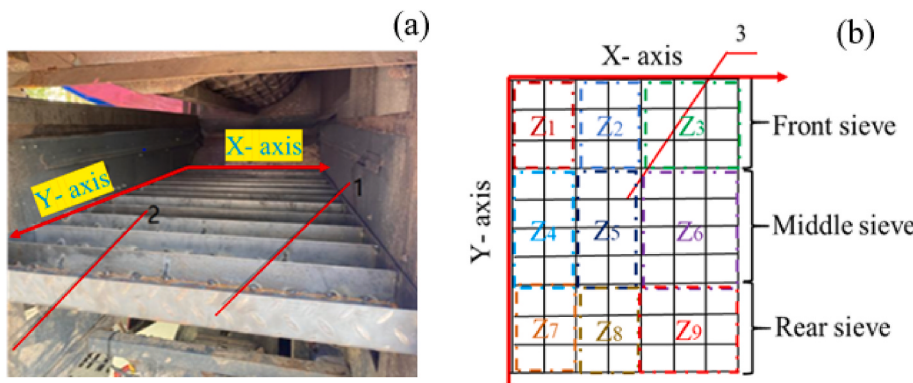


Fig. 2. Receiving box installation method and arrangement: (a) receiving box installation inside the combine harvester (1 – holder, 2 – cleaning shoe wall); and (b) receiving box arrangement separated into a 10 × 7 matrix, forming nine measurement zones (Z_1 – Z_9), 3 – receiving box.

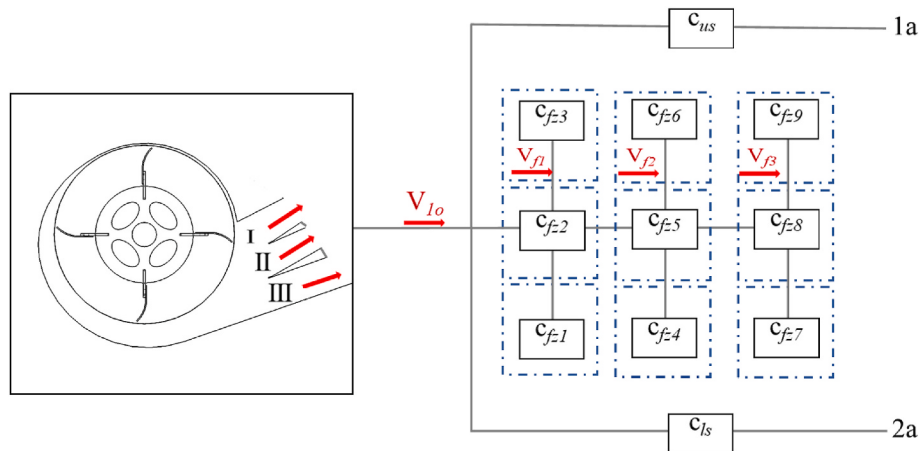


Fig. 3. Airflow resistance distribution within the cleaning shoe; c_{us} and c_{ls} - the resistance due to upper and lower sieves, $c_{fz1}, c_{fz2}, c_{fz3}, c_{fz4}, c_{fz5}, c_{fz6}, c_{fz7}, c_{fz8}$ and c_{fz9} - the resistances due to fluidised grain from Zone 1 to 9, V_{Io} - fan outlet velocity from Duct I, II, and III, V_{f1}, V_{f2} , and V_{f3} - the minimum fluidisation velocity at front, middle and rear sieve sections, 1a, 2a - pressures at the atmospheric conditions.

along the airstream inside the channel. Therefore, the force exerted by the pressure difference should not exceed the gravitational force of the material's mass. The pressure difference between the lower and upper surfaces of the layer becomes the pressure drop (ΔP), the ΔP is a function of the density of the fluidised grain (ρ_f) and the height of the grain mat above the sieve surface, and it can be calculated using Eq. (1) (Zhao & Wu, 1989). Grain mat resistance refers to the resistance encountered by airflow as it moves through the layer of grain positioned between the lower and upper surfaces of the sieve. The resistance coefficients, due to the fluidised grain for each zone (c_{fz}), are calculated using Eqs. (1)–(4) (Zhao & Wu, 1989).

$$\Delta P = (\rho_g - \rho_a)(1 - \varepsilon_f)gH_f \quad (1)$$

$$\rho_f = (1 - \varepsilon_f)\rho_g \quad (2)$$

$$H_f = \frac{M_f}{\rho_f A_z} \quad (3)$$

$$c_{fz} = \frac{(\rho_g - \rho_a)(1 - \varepsilon_f)gH_f}{\frac{1}{2}\rho_a V_f^2} \quad (4)$$

where, ΔP is the static pressure drop, Pa; H_f is the height of fluidised grain mat, m; M_f is the mass of grain in each zone, kg; A_z is the area of the sieve in each zone, m^2 ; V_f is the fluidisation velocity, $m s^{-1}$; ρ_g is the bulk density of fluidised grain, 1350 kg m^{-3} ; ρ_a is the density of air, 1.225 kg m^{-3} ; g is the gravitational acceleration, 9.81 m s^{-2} ; and ε_f is the porosity of a fluidised grain mat, usually $\varepsilon_f = 40\text{--}60\%$, c_{fz} is the coefficient of resistance, which is the ratio of the static pressure drop (ΔP) to the dynamic pressure.

The dynamic pressure can be calculated by Eq. (5).

$$q = \frac{1}{2}\rho_a V_f^2 \quad (5)$$

where, q is the dynamic pressure, Pa; V_f is the fluidisation velocity, $m s^{-1}$ and ρ_a is the air density, kg m^{-3} .

2.3.2. Resistance due to the cleaning sieve

The sieve is another component that induces resistance as airflow passes through its perforations. In the reference combine harvester, the sieve consists of a dual-layer arrangement, with adjustable louvers as the upper sieve and a woven sieve as the lower sieve (see Fig. 1(a)). Airflow resistance is contributed by both the louver (upper) and woven (lower) sieves, and the resistance of the upper sieve to airflow is directly related to the size of the sieve opening, as illustrated in Fig. 4. The sieve opening

ratio (λ) is the ratio of the sieve open area (A_0) to the total area of the sieve (A_t). A larger λ results in a lower airflow resistance, while smaller sieve openings increase airflow resistance. The λ can be calculated using Eq. (6).

$$\lambda = \frac{A_0}{A_t} = \frac{(h \times l)}{(d \times l)} = \frac{d \times \sin \theta \times l}{d \times l} = \sin \theta \quad (6)$$

where, l is the length of the chaffer sieve plate, mm; d is the distance, mm; and θ is the sieve opening angle, $^\circ$.

It has been observed that the performance of the cleaning system can meet the relevant national standard in the case of a chaffer sieve λ of 60–80 % (Gebrehiwot, 2010b). A woven sieve with an effective opening ratio of $\lambda = 90\%$, the resistance due to the upper sieve (c_{us}) and lower sieve (c_{ls}), can be calculated using Eq. (7).

$$c_s = 1.3(1 - \lambda) + \left(\frac{1}{\lambda} - 1 \right)^2 \quad (7)$$

where, c_s is the resistance due to the cleaning sieve, λ is the sieve opening, mm

2.3.3. Resistance in each zone within the cleaning shoe

The airflow resistance coefficient (c_f) in each zone is the combined resistance resulting from the fluidised grain mat and the resistances of both the cleaning sieves in that specific zone, as described by Eq. (8). This summation of resistances accounts for the varying material and sieve properties in each region of the cleaning system, influencing the overall airflow distribution and pressure drop across the cleaning shoe.

$$c_f = \sum_{z=1}^n c_{fz} + c_{ls} + c_{us}; n = 1, 2, 3, \dots, 9 \quad (8)$$

where, c_f is the airflow resistance in each zone, c_{fz} is the airflow resistance due to fluidised grain in each zone, c_{ls} is the airflow resistance due to lower sieve in each zone, c_{us} is the airflow resistance due to upper sieve in each zone, n is the number of measurement zones.

2.3.4. Design of the perforated plates according to the resistance in each zone

According to the calculated airflow resistance in different zones, the perforated plates are manufactured to simulate the working load of the fan. The perforated plate airflow resistance and open area ratio can be calculated using Eqs. (9) and (10), as suggested by Idelchik (2008), and the schematic diagram of the perforated plate is shown in Fig. 5.

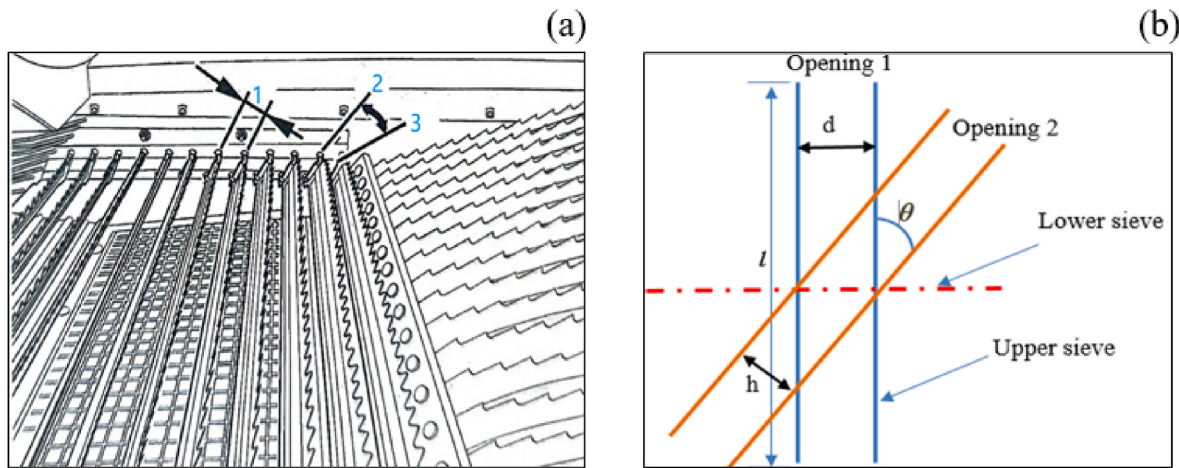


Fig. 4. Resistance due to upper sieves; 1 - sieve opening, 2 - fully opened, 3 - fully closed, 1 - length of chaffer sieve plate, d - the distance between adjacent fish scale sieve, θ - the sieve opening angle, h - sieve opening.

$$c_f = [0.707(1 - \beta)^{0.375} + 1 - \beta]^2 \frac{1}{\beta^2} \quad (9)$$

$$\beta = \frac{d^2 \times 90.69}{c^2} \quad (10)$$

where, β is the perforated plate open area ratio, %; d is the diameter of perforations in the plate, mm; and c is the centre distance between 60° staggered holes, mm.

The pressure drop (ΔP) across the perforated plate can be calculated by using Eq. (11). It is a function of the total resistance coefficients for each plate and the dynamic pressure based on the freestream velocity as described by Idelchik (2008).

$$\Delta P = c_f \rho_a v^2 \quad (11)$$

where, ΔP is the pressure drop, Pa; c_f is the calculated airflow resistance in different zones; ρ_a is the density of air, kg m^{-3} , $\rho_a = 1.225 \text{ kg m}^{-3}$ and v is the airflow velocity, m s^{-1} .

2.4. Computational method- CFD simulation

In this study, a CFD simulation is conducted and the airflow velocity

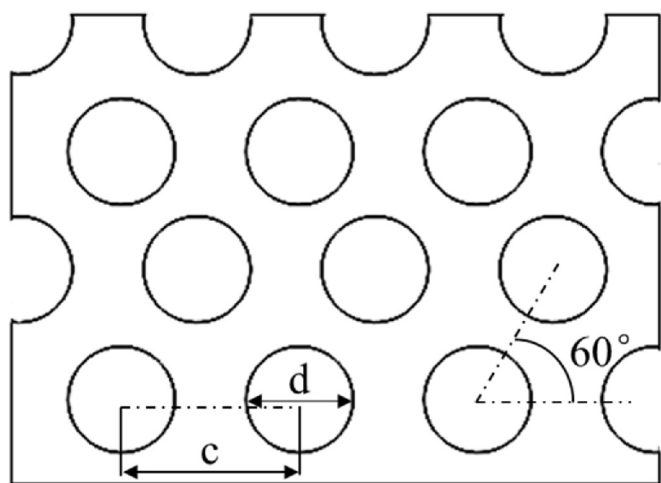


Fig. 5. Perforated plate open area calculation method; c - centre distance between holes, d - diameter of holes, and 60° is the angle of staggered arrangement of holes.

and pressure at the fan ducts and inside the fan are analysed by incorporating a porous media with different resistance value as the working load. The simulation results are validated by comparing them with a hot wire anemometer (HWA) measurement (Gebrehiwot et al., 2010a). Subsequently, the effects of varying working loads on the airflow velocity at the fan outlets and the pressure distribution inside the fan are investigated. This simulation also helps to identify performance limitations of the existing fan under different conditions.

2.4.1. Geometric model and mesh generation

The geometric model is developed using SolidWorks® 2023 (Dassault Systèmes S.A., Paris, France), and it consists of two zones: the moving zone (the fan) and the stationary zone. To optimise computational resources, only half of the domain width is simulated, taking the cleaning shoe's symmetrical design (Gebrehiwot et al., 2010a). In the CFD simulation, perforated plates with a thickness of 2 mm are used to represent the cleaning load as shown in Fig. 6(a). The pressure drop is defined as a porous medium. Pre-processing and grid generation are performed using ICEMCFD 2021 R1 software (ANSYS Inc., Canonsburg, PA, USA). Due to the high velocities, complex geometry, and the presence of threshed materials inside the cleaning shoe, the airflow is predominantly turbulent, making the calculations unsteady. To address this, an unstructured tetrahedral meshing technique is applied to establish a sliding mesh configuration. The presence of fine pores in the perforated plates made direct meshing challenging and would have resulted in an excessive number of computational cells. Therefore, a numerical model is used to simulate the effects of airflow through the perforated plates. The discretised model, based on the finite volume method, consists of a total of 5,169,269 tetrahedral elements, as shown in Fig. 6(b).

2.4.2. CFD simulation setup and incorporation of porous media

Since the airflow inside the cleaning shoe is highly transient, steady-state calculations can lead to significant errors (Xu et al., 2015), and the complex geometry makes achieving convergence challenging. To mitigate this problem, the solution was first initialised with steady flow using the multiple reference frame (MRF) technique and first-order discretisation (FOD) schemes, then switched to transient flow analysis (Seo et al., 2003). In the calculations, the Reynolds continuity equation, Navier-Stokes equations, and the RNG $k-\epsilon$ turbulence model are employed (Ji et al., 2017). The fan domain is defined as a moving zone with rotational speeds of 1300 rpm and 1500 rpm, while the perforated plates are modeled as porous zones to simulate various working loads, characterised by different permeability, inertial resistance, and porosity values, as shown in Fig. 6.

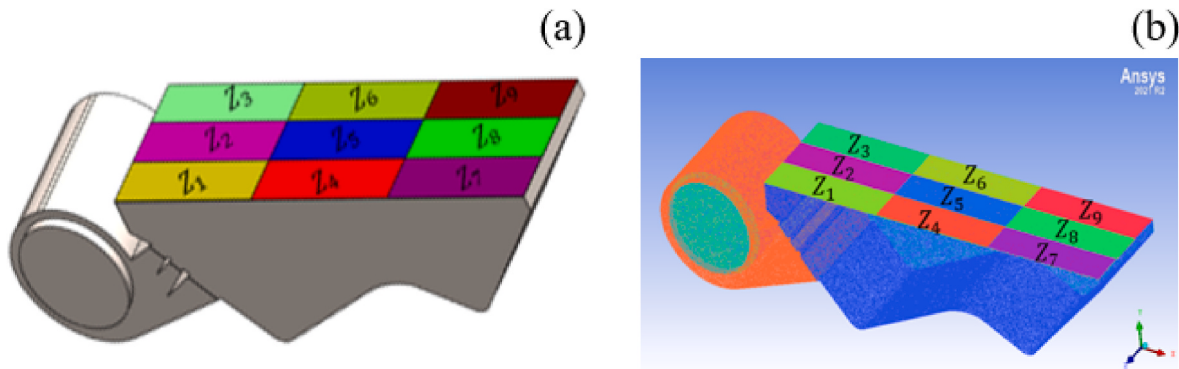


Fig. 6. Computational model of the cleaning system (Z_1 - Z_9 are nine different porous zones); (a) Geometric model, and (b) Mesh generation.

The pressure-drop (ΔP) source term consists of two components: a viscous loss term and an inertial loss term (FLUENT Inc, 2006). From Eq. (12), the Darcy term, the first term on the right-hand side (RHS), corresponds to the viscous pressure loss, while the second term represents the inertial pressure loss. To determine the permeability (α) and the inertial resistance coefficient (c_2) of the porous media, experimental data for the pressure drop and airflow velocity are plotted and fitted to Eq. (13) (Gebrehiwot et al., 2010a). From this equation, the coefficient A_1 (viscous resistance) ($\frac{1}{\alpha} = \frac{A_1}{\mu\delta}$), and the coefficient B_1 (inertial resistance) ($c_2 = \frac{2B_1}{\rho\delta}$) are obtained.

$$\Delta P = \frac{\mu}{\alpha} \delta v + c_2 \frac{1}{Z} \rho_a \delta v^2 \quad (12)$$

$$\Delta P = A_1 v + B_1 v^2 \quad (13)$$

where, ∇P is the pressure gradient, Pa m^{-1} ; ΔP is the pressure drop, Pa ; α is the permeability of the porous media, m^2 ; δ is the thickness of porous media, mm ; c_2 is the inertia resistance coefficient, m^{-1} , ρ_a is the air density, kg m^{-3} , 1.225 kg m^{-3} ; v is the free stream velocity, m s^{-1} and μ is the dynamic viscosity of the fluid, Pa s , $\mu = 1.7894 \times 10^{-5} \text{ Pa s}$.

The fan inlet is defined as a pressure inlet, and the outlets are set as pressure outlets with values of 0 Pa (Yu, 2015). Pressure correction is performed using the SIMPLE algorithm, and convergence is achieved when the relaxation factor is set as fluent default and the residual is set to 0.0001. All necessary boundary conditions are applied, including inlets, rotating fan blades, interfaces between rotating and stationary regions, symmetrical walls, volute wall, cleaning shoe wall, porous

regions, and outlets. Unsteady calculations are carried out over 250 time steps, with a time step size of $3.67 \times 10^{-5} \text{ s}$, resulting in total of 12,000 iterations.

2.5. Validation of the CFD simulation

The CFD simulation is carried out at the guide plate angles I & II of 42° , with fan revolution speeds of 1300 rpm and 1500 rpm, and a feed rate of 6 kg s^{-1} . Setting the relevant resistance in the CFD model, simulations are carried out and the airflow velocity at certain points is obtained.

To verify the CFD simulation results, the cleaning sieve is removed and replaced with perforated plates as shown in Fig. 7(b). Airflow measurement holes are then drilled at multiple points on the cleaning shoe wall, allowing for the insertion of a HWA to obtain precise airflow velocity measurements below the perforated plates. Measurement points are: four positions along the Y-axis at 150, 400, 650, and 900 mm along the longitudinal sieve length; six positions along the X-axis at symmetrical intervals of 125, 250, and 375 mm across the transverse sieve width; and two layers were positioned along the Z-axis at 50 and 150 mm below the perforated plate, as shown in Fig. 7(a). Airflow velocity is measured at these points below the perforated plates using a HWA (VT100, KIMO, Paris, France) with a measurement range from 0.15 to 30 m s^{-1} with an accuracy of $\pm 0.05 \text{ m s}^{-1}$ and a resolution of 0.01 m s^{-1} . The rotational speed of the fan is measured with a digital tachometer (HT-4200, Ono Sokki Technology, Inc., Tokyo, Japan) with a measurement range of 30–50,000 rpm. Each airflow velocity measurement is repeated three times, and the average value is taken as the final result. After post-processing the solution, the CFD simulation results are

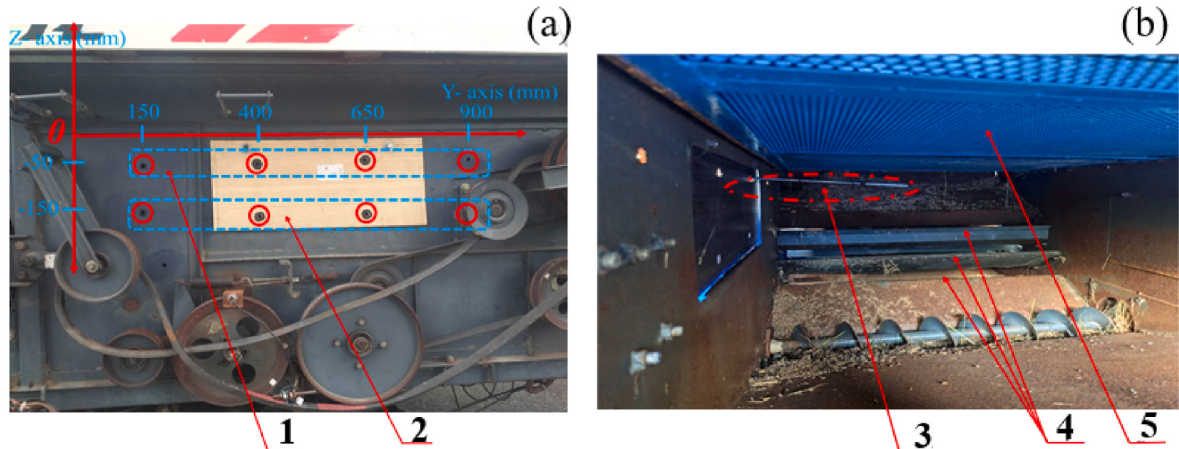


Fig. 7. Airflow velocity test points in the cleaning shoe of the combine harvester; (a) Measuring points, 1 - upper measurement layer, 2 - lower measurement layer, and (b) HWA-airflow velocity measurement method, 3 - HWA, 4 - the three fan ducts (Duct I, Duct II and Duct III), 5 - installed perforated plate.

validated by comparing them with measurements from the HWA to verify the accuracy of the simulation model. This validation involved plotting velocity profiles and calculating the RMSE using Eq. (14).

$$\text{RMSE} = \sqrt{\frac{1}{n} \sum_{i=1}^n (V_{\text{Mea}} - V_{\text{CFD}})^2} \quad (14)$$

where, V_{Mea} is the measured airflow velocity at a specific point, m s^{-1} , V_{CFD} is the predicted simulation values of airflow velocity at a specific point, m s^{-1} , and n is the number of observations.

2.6. Working parameters optimisation for the cleaning system

After validation of the CFD simulation model, it is then used to analyse the variations in airflow velocity at the fan outlet and the total pressure distribution inside the fan under different operational parameter settings. The main operational parameters of the combine harvester are fan speed, guide plate angle, sieve opening (Li et al., 2018). A design of experiments (DOE) approach is employed by varying key fan working parameters and using the CFD simulation model to identify optimal settings. This study focuses on specifically optimising the guide plate angles, fan speed, and sieve openings. The Box-Behnken Design (BBD) and Response Surface Methodology (RSM) statistical techniques are used to optimise the fan's working parameters as detailed in Table 1.

Based on a comprehensive analysis of the CFD simulation results, a specific combination of working parameters is identified that can significantly improve airflow velocity at the fan outlet and ensure ideal pressure distribution. In addition, the simulation results are then plotted as a graph of total resistance coefficient (c_f) versus airflow volume rate Q ($\text{m}^3 \text{s}^{-1}$) and compared with the fan's performance curve to pinpoint areas for potential improvement. For a fan operating in a combine harvester, the total pressure (ΔP_{tot}) must be sufficient to fluidise the material layer, which can vary significantly over time, while requiring only minor adjustments from the operator during harvesting operation. A steeper slope in the performance curve indicates better fan efficiency, as it demonstrates the ability to maintain higher airflow rates with less resistance.

2.7. Field experimental validation of optimised settings

This optimal setting is experimentally verified by investigating grain sieve loss and grain impurity ratios under field tests, shown in Fig. 8(a). A perforated plastic bag is used to collect all sieve outputs, as illustrated in Fig. 8(b), then, the rice grains are isolated from the mixture using a re-cleaner (Agriculex ASC-3 Seed Cleaner, Guelph, ON, Canada) and weighed, respectively, to calculate the grain loss ratio. The grain impurity ratio is calculated by sampling from the grain tank (1 kg with an accuracy of ± 1 g) according to the national standard in China, DG/T 014–2009 (Ministry of Agriculture of the People's Republic of China, 2009). According to Chinese national standards (JB/T 5117-2006), the acceptable grain sieve loss is $<1\%$, and grain impurity ratio should be $<2\%$.

Table 1
Design Of Experiment for fan working parameter optimisation.

| Conditions | Guide plate angle (I) ($^\circ$) | Guide plate angle (II) ($^\circ$) | Sieve opening (mm) | Fan speed (rpm) |
|------------|------------------------------------|-------------------------------------|--------------------|-----------------|
| 1 | 30 | 28 | 22 | 1100 |
| 2 | 34 | 30 | 26 | 1100 |
| 3 | 30 | 28 | 30 | 1100 |
| 4 | 38 | 36 | 26 | 1300 |
| 5 | 34 | 30 | 22 | 1300 |
| 6 | 38 | 36 | 30 | 1300 |
| 7 | 30 | 28 | 26 | 1500 |
| 8 | 34 | 30 | 30 | 1500 |
| 9 | 38 | 36 | 22 | 1500 |

The fan revolution speed can be adapted by changing the corresponding drive wheel diameter and adjusting the tensioning mechanism. The harvested rice crop variety in the field test is Yangnong No. 1 with an average height of 850 mm, straw/grain ratio is 2.0 and an average stubble length of 17 mm. The average one-thousand kernel weight is 30 g and the average grain yield is 7400 kg ha^{-1} . The average moisture content is respectively 76.5 % and 22.5 % for straw and grain. The grain sieve loss and grain impurity ratio are calculated as outlined below:

For grain sieve loss, G_l (%):

$$G_l = \frac{w_g}{w} \times 100\% \quad (15)$$

where, w_g is the mass of the collected grains in the perforated bag, g; w is the grain mass in grain tank, g.

For grain impurity ratio, I_m (%):

$$I_m = \frac{MOG_T}{w} \times 100\% \quad (16)$$

where, MOG_T is the MOG mass in the grain sample, g; w is the grain sample mass, g.

3. Results and discussion

3.1. Analysis of the threshed output distribution

The distribution of the threshing outputs on the cleaning shoe had a significant impact on the cleaning performance. The sieve was divided into front, middle, and rear sections, as illustrated in Fig. 2(b). The analysis revealed a significant variation in the working load along the longitudinal direction of the sieve. In the front section of the cleaning sieve (0–450 mm), the grain mass accounted for 61 % of the total threshed grain mass. In the middle section (450–1050 mm), it accounted for 34.4 %, while in the rear section (1050–1500 mm), it represented only 4.60 % of the total mass. This analysis showed that the grain mass gradually decreased along the length of the cleaning sieve. Moreover, the grain distribution across the width of the sieve was also uneven, exhibiting a pattern of higher accumulation on both sides and lower accumulation in the centre. Areas in the front section of the sieve, where material accumulation was greater, required significantly more energy to maintain grain fluidisation compared to regions with thinner layers. This finding aligned with the work of Korn et al. (2013), and indicated that the front section of the chaffer sieve had a higher material layer and produced greater airflow resistance. Additionally, it was consistent with the finding made by Liang et al. (2022), who noted that after the threshing cylinder completed its function, the output was unevenly distributed across the vibrating screen, with a higher concentration of material at the front and lower concentration at the back. From Fig. 9(a) it can be observed that, by mass, grains accounted for 88 %–95 % of the threshed output in each zone of the front section. In the middle section, grains comprised 64 %–86 % of the material in each zone, whereas in the rear section, which was considerably thinner, grains represented only about 18 %–26 % of each zone. This increased grain accumulation in the front section obstructed airflow, resulting in higher airflow resistance and requiring a greater pressure to fluidise the grains. The thicker grain layers in the front section not only hindered airflow but also reduced the efficiency of separating grain from the MOG. As a result, the uneven distribution of the grains compromised the overall effectiveness of the cleaning process, particularly in separating grain from MOG.

Similarly, as shown in Fig. 9(b), the rear section of the sieve exhibited a substantially higher accumulation of MOG, with its mass share reaching 57 %–82 % in each zone, compared to the front and middle sections, which accumulated 8 %–10 % and 16 %–44 % in each zone, respectively. This high accumulation of MOG with high moisture content required more energy for effective removal from the cleaning shoe.



Fig. 8. Field experiment on grain loss and impurity ratio; (a) Experimental setup, 1 - pole, 2 - Combine harvester, and (b) Grain loss collection, 3 - Oilskin, 4 - Perforated bag.

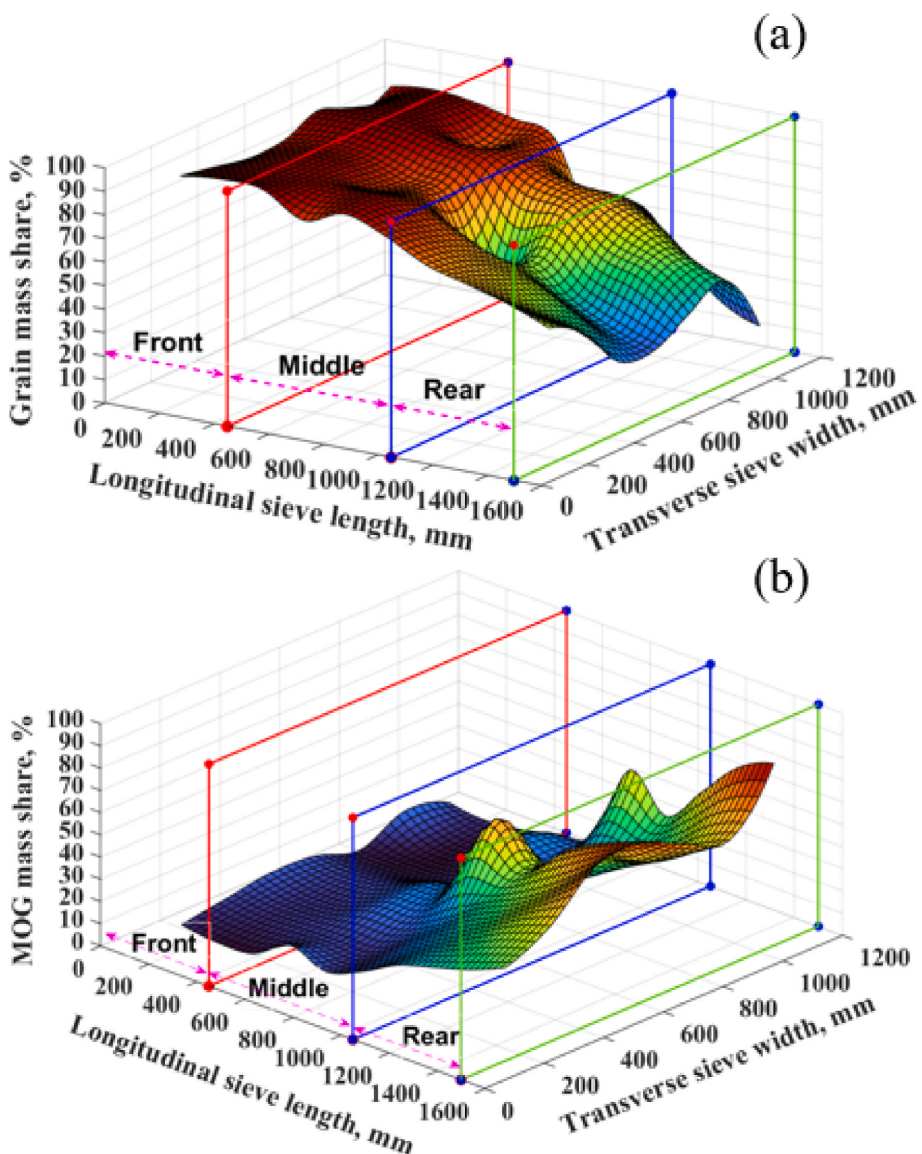


Fig. 9. Threshed output distribution across sieve zones; (a) Grain mass share, and (b) MOG mass share.

When the cleaning shoe was severely overloaded, the airflow velocity delivered by the cleaning fans was insufficient to keep the grain and MOG fluidised, leading to inefficiencies in the cleaning process and

negatively affecting overall performance. As the fan is the source of the airflow for the cleaning shoe, optimising airflow velocity and pressure distribution inside the fan is crucial for providing the necessary airflow

to achieve effective grain fluidisation and removal of MOG.

3.2. Analysis of the resistances to airflow

3.2.1. Resistance due to fluidised grain

Fluidised grain significantly resisted airflow in the cleaning system of the combine harvester, as its accumulation can create substantial obstructions within the sieve. This buildup not only hindered the efficient movement of airflow necessary for effective separation of grain from foreign materials but also increased the pressure required to maintain optimal airflow. Thus, knowing the resistance due to fluidised grain at different zones is essential for optimising the cleaning process and improving overall harvesting efficiency. The resistances of the grain mat, collected from nine measurement zones of the sieve section during the threshed output collection experiment described in Section 2.2, were analysed. Firstly, the mass of fluidised grain (M_{fz}) of the nine zones was calculated according to threshed output distribution. Then, the density of fluidised grain (ρ_f) was calculated using Eq. (2) by assuming a grain porosity of (ϵ_f) = 40 % for fluidised grain and a bulk density of grain (ρ_g) = 1350 kg m⁻³, leading to the determination of the height of the fluidised grain above the sieve section (H_{fz}) accordingly to Eq. (3). The corresponding grain mass (M_{fz}) and mat layer thickness (H_{fz}) for the nine sieve zones are presented in Fig. 10.

According to Fig. 10, the height of the grain mat increased slightly with the feed rate. However, the grain distribution across different regions showed no significant variation under varying feed rates. Zones 1, 2, 3, and 6 exhibited relatively higher grain layer heights, which directly influenced the static air pressure beneath the material and increased airflow resistance. In contrast, Zones 7, 8, and 9 had the lowest grain layer heights. Both airflow pressure and resistance were proportional to the thickness of the grain mat, meaning thicker layers required more energy for fluidisation and increased the demand for effective airflow management within the cleaning system. To achieve a better cleaning performance, the fan must provide sufficient airflow pressure to break

up the highly accumulated material layer and fluidise the grain in the front sieve section. The required pressure drop (ΔP) at the bottom of the grain mat was influenced by factors such as grain density (ρ_g), air density (ρ_a), porosity (ϵ_f), height of the fluidised grain mat (H_{fz}), and gravitational acceleration (g). The ΔP can be calculated with Eq. (1), and the results are presented in Fig. 11.

From Fig. 11, it can be seen that the sieve became overloaded, resulting in a significant pressure drop in the front sieve section, ranging from 197.76 to 276.97 Pa. In the middle sieve section, the pressure drop was measured at 142.00–38.00 Pa, while the rear sieve section experienced a much lower pressure drop, ranging from 25.58 to 5.59 Pa. The highest pressure drop (ΔP) occurred in the front sieve section, suggesting that this area required considerable airflow energy to achieve effective fluidisation. Several factors contributed to this phenomenon, including the properties of the grain mat, grain mat thickness, density and porosity in this region. This variation in pressure drop across the sieve sections indicated differing airflow dynamics and highlights the inefficiencies in the cleaning process, particularly in the overloaded front section.

The resistance coefficient of fluidised grain mat to airflow (c_f) for each sieve zone section was calculated as the ratio of the pressure drop across the sieve zone area to the dynamic pressure. The dynamic pressure (q) at the cleaning sieve surface represents the pressure exerted by the moving air and is given by the equation, $q = \frac{1}{2} \rho_a V_f^2$. This pressure is essential for effective grain separation, as it helps fluidise the material on the sieve and carry away lighter particles such as chaff while allowing the grain to settle. The upstream airflow velocities from the existing cleaning fan outlets at the front, middle, and rear sieve sections were measured using an HWA. The air velocity from Duct I (V_{f1}) ranged from 3.20 to 7.50 m s⁻¹, from Duct II (V_{f2}) was 8.45–10.25 m s⁻¹, and from Duct III (V_{f3}) was 13.25–15.85 m s⁻¹ (see Fig. 1(b) for the duct arrangements). Consequently, the resistance coefficients due to the fluidised grain mat (c_f) were determined by using Eq. (4). The calculated resistance coefficients for each zone and the values are detailed in Table 2. It is evident from Table 2 that the height of the fluidised grain decreased from the front to the rear of the sieve section, and also the front section was characterised by lower porosity and higher density, and exhibited a higher resistance coefficient. Thus, the front sieve sections showed the highest resistance coefficient ($c_f = 2.63–7.66$), indicating the greatest resistance to airflow due to a higher accumulation of material and lower porosity. Whereas, the middle sieve section had a lower resistance coefficient ($c_f = 0.53–2.28$), suggesting moderate airflow resistance and more efficient separation. The rear sieve zones had the lowest resistance coefficient ($c_f = 0.04–0.17$), reflecting minimal resistance to airflow, likely due to a reduced load of material.

3.2.2. Resistance due to the cleaning sieves (c_{ls})

The size of the cleaning sieve openings significantly influenced airflow resistance in the combine harvester's cleaning system. Larger openings facilitated a greater flow of air, allowing for more effective separation of grain from impurities by reducing resistance and minimising pressure drops. This enhanced airflow helped to maintain optimal cleaning performance, as it promoted the rapid movement of chaff and other foreign materials away from the grain. Conversely, smaller sieve openings created increased resistance, restricting airflow and leading to higher pressure drops across the sieve. While smaller openings may improve the retention of smaller impurities, they can also result in inefficient cleaning and higher energy demands on the fan to achieve the necessary airflow rates. Therefore, striking a balance between the sizes of sieve openings is crucial for optimising airflow velocity and ensuring effective cleaning performance, ultimately impacting the overall efficiency of the harvesting process. Accordingly, the resistance to airflow due to the lower sieve (c_{ls}) was calculated by using Eq. (6) and it was found that $c_{ls} = 0.14$. The resistance due to the upper sieve was assessed by testing three different sieve openings, 22,

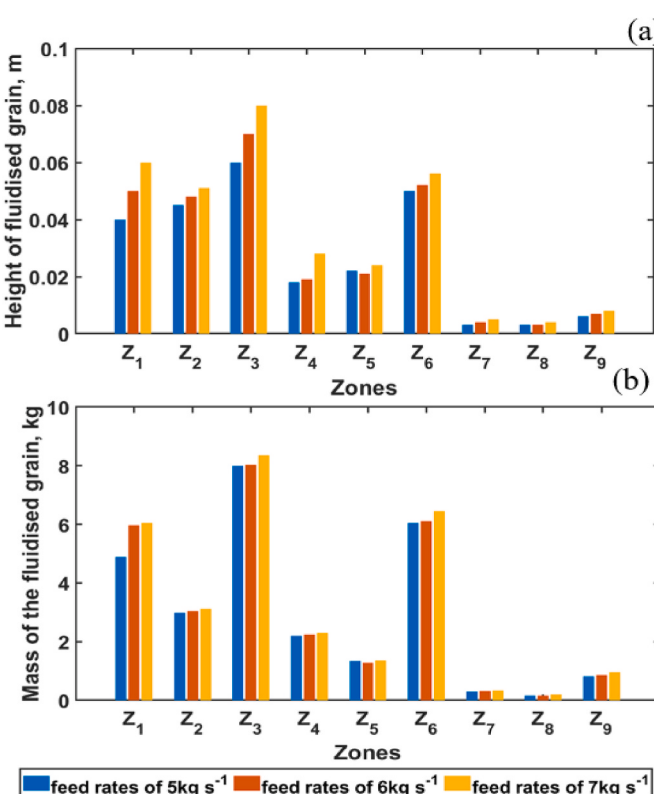


Fig. 10. The distribution of fluidised grain mass and grain mat layer thickness in each zone; (a) Height of fluidised grain, and (b) Mass of the fluidised grain.

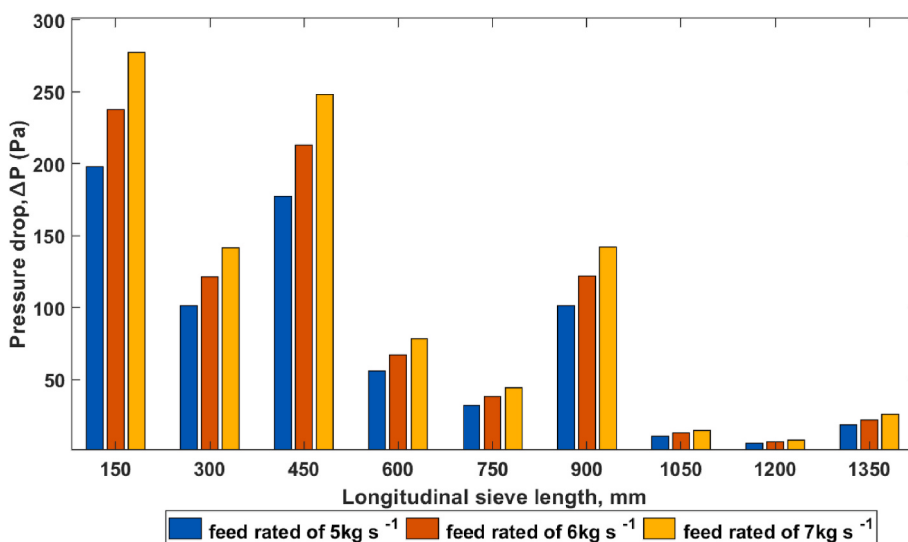


Fig. 11. Pressure drop (ΔP) at different feed rates along the sieve length direction.

Table 2

The resistance due to fluidised grain (c_f) in each zone.

| Feed rates (kg s^{-1}) | Zones | | | | | | | | |
|-----------------------------------|----------------|----------------|----------------|----------------|----------------|----------------|----------------|----------------|----------------|
| | Z ₁ | Z ₂ | Z ₃ | Z ₄ | Z ₅ | Z ₆ | Z ₇ | Z ₈ | Z ₉ |
| 5 | 5.48 | 2.63 | 4.34 | 0.99 | 0.53 | 1.63 | 0.07 | 0.04 | 0.12 |
| 6 | 6.57 | 3.16 | 5.21 | 1.19 | 0.64 | 1.96 | 0.09 | 0.04 | 0.14 |
| 7 | 7.66 | 3.69 | 6.08 | 1.38 | 0.75 | 2.28 | 0.10 | 0.05 | 0.17 |

26, and 30 mm, and yielded resistance coefficients of $c_{ls} = 0.96$, 0.57, and 0.32, respectively. Therefore, the total resistance coefficient (c_f) is the sum of resistance due to the fluidised grain mat and the resistance from the cleaning sieves, as detailed in Table 3.

Based on the calculated total resistance coefficient, appropriate perforated plates with varying opening ratios were selected for the nine zones as detailed in Table 4. Round-hole perforated plates were chosen for their versatility, replacing the cleaning sieve during both measurement and simulation phases, as shown in Fig. 12. The perforated plates were designed to achieve resistance values recommended by Idelchik (2008). Their open area ratio (porosity) was calculated using Eq. (19) (Collar, 1939).

$$c_f = k \frac{(1 - \beta)}{\beta^2} \quad (19)$$

where, c_f is the total resistance coefficient; k is an empirical constant depending on the type of perforation (round holes in this case), and β is the porosity or opening ratio of the perforated plate (ratio of open area to total area).

To validate the CFD simulated model, this study employed guide plate angles I and II set at 42° , along with fan revolution speeds of 1300 and 1500 rpm. The feed rate was maintained at 6 kg s^{-1} , and the corresponding perforated plate opening ratio for the fan parameter settings is detailed in Table 4.

Table 3

Total resistance at different feed rate and sieve openings for fan outlets.

| Resistance source | Symbol | Feed rates (kg s^{-1}) | | |
|---------------------------------|----------|-----------------------------------|-----------|-----------|
| | | 5 | 6 | 7 |
| Resistance from fluidised grain | c_f | 0.04–5.48 | 0.04–6.57 | 0.05–7.66 |
| Resistance from upper sieve | c_{us} | 0.32–0.96 | 0.32–0.96 | 0.32–0.96 |
| Resistance from lower sieve | c_{ls} | 0.14 | 0.14 | 0.14 |

According to the calculated resistance range, the perforated plates were manufactured with different opening ratios to approach the above opening ratio as shown in Fig. 12.

These plates were arranged to serve as a substitute for the combine harvester's cleaning sieve, effectively simulating the actual fan loads experienced during operation. To ensure structural integrity during measurements, the perforated plates were arranged and securely fixed to the cleaning shoe wall of the combine harvester, as shown in Fig. 13(a) and (b), to maintain stability and accuracy throughout the testing process.

Details of the total pressure drop (ΔP) along the longitudinal sieve length can be found in Fig. 14. The highest pressure drop of 317.00 Pa was recorded at the front sieve of Zone 1, with a feed rate of 7 kg s^{-1} and a sieve opening of 22 mm, where the grain mat height reached 0.035 m. This maximum value was attributed to the thicker material layer in this zone compared to others, thus the airflow resistance increased, and it requires a high amount of airflow energy during grain cleaning operation.

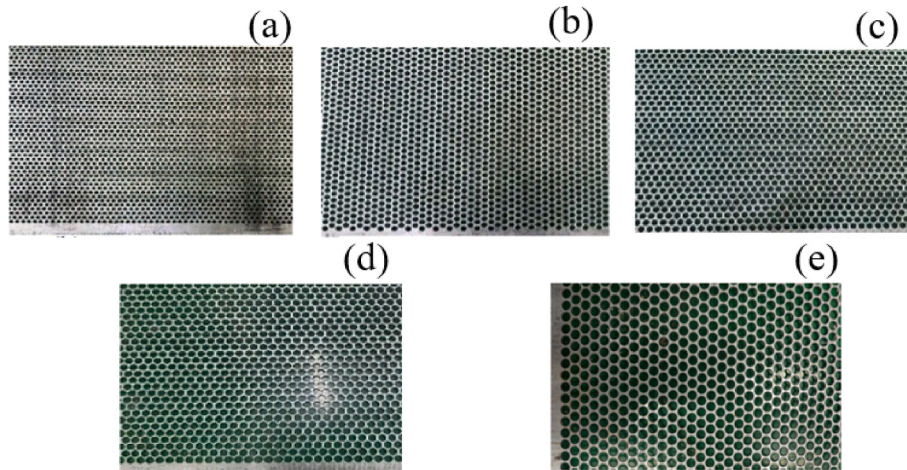
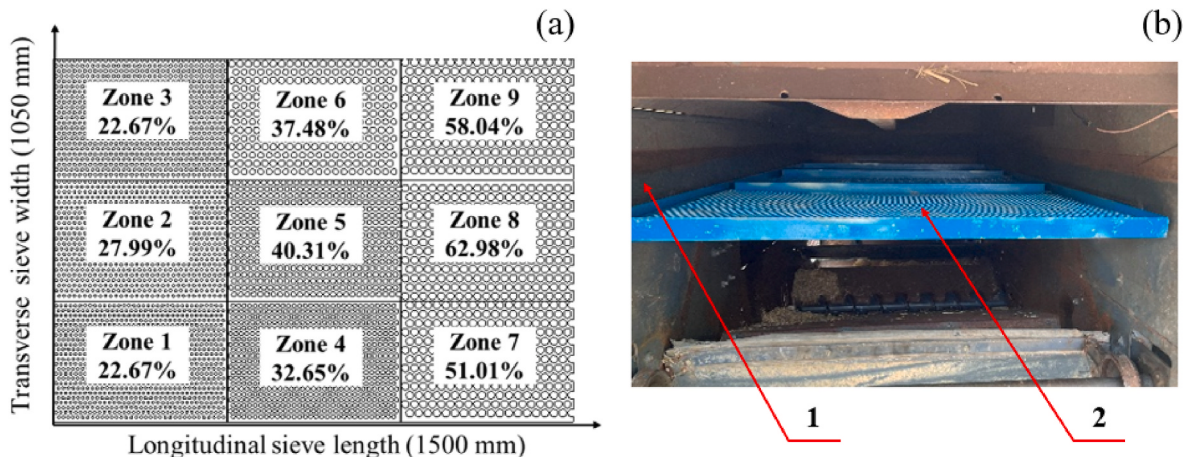
The pressure drop is directly related to material thickness and porosity. Among all the test combinations, No.7, which consisted of a feed rate of 5 kg s^{-1} and a sieve opening of 22 mm, exhibited the highest pressure drop. This significant pressure drop indicated that the selected parameters created substantial airflow resistance within the cleaning system, potentially affecting the efficiency of grain separation. The sieve opening which may restrict airflow when the openings are smaller. Together, these factors necessitate a higher pressure to maintain effective fluidisation.

3.3. Airflow velocity distribution below the perforated plates and validation of CFD simulations

The air velocity distributions were measured at multiple points below the perforated plate. The airflow velocity increased both along the longitudinal direction of the sieve and with increasing distance from

Table 4Perforated plates opening ratios (porosity - β).

| Symbol | Zones | Z_1 | Z_2 | Z_3 | Z_4 | Z_5 | Z_6 | Z_7 | Z_8 | Z_9 |
|---------|-------|-------|-------|-------|-------|-------|-------|-------|-------|-------|
| c_f | | 6.57 | 3.16 | 5.21 | 1.19 | 0.64 | 1.96 | 0.09 | 0.04 | 0.14 |
| β | | 0.29 | 0.40 | 0.30 | 0.51 | 0.60 | 0.61 | 0.65 | 0.64 | 0.65 |

**Fig. 12.** Manufactured perforated plate with different opening ratios; (a) Opening ratio = 29.61 % (d = 4, c = 7), (b) Opening ratio = 40.31 % (d = 8, c = 12), (c) Opening ratio = 51.01 % (d = 9, c = 12), (d) Opening ratio = 60.71 % (d = 9, c = 11), and (e) Opening ratio = 64.93 % (d = 11, c = 13).**Fig. 13.** Arrangement of perforated plates and the location within the cleaning shoe; (a) Perforated plate arrangement, and (b) Assembly of perforated plate in cleaning shoe, 1- cleaning shoe wall, 2- perforated plates.

the perforated plate. In all measurements as shown in Fig. 15(a) and (c), the airflow velocity at the front sieve section was consistently in between 2.5 and 4.25 m s⁻¹. From Fig. 15(d), it can be seen that on the plane located 150 mm below the perforated plates, and with a fan rotational speed of 1500 rpm, the maximum airflow velocity recorded in the front sieve section ranged from 2.5 to 4.25 m s⁻¹, while in the middle sieve section, it ranged from 4.5 to 8 m s⁻¹. In contrast, the rear section of the sieve exhibited a significantly higher airflow velocity, ranging from 9.5 to 14 m s⁻¹.

The airflow velocity data from the CFD simulations were plotted alongside the measured airflow values obtained from the HWA at the same coordinates to assess the validity of the CFD simulations, as were shown in Fig. 16. The velocity profiles of the measured and simulated airflow were compared by calculating the RMSE. The results indicated a good match between the simulated and measured velocities, with RMSE

values ranging from 0.1 to 0.36 m s⁻¹ and similar trends observed along the sieve length. Since the percentage error remained below the 5 % threshold, this suggested that the CFD model provided a reliable representation of real-world conditions, meeting the validation criteria necessary for accurate analysis and optimisation of fan performance.

3.4. Effects of working load variations on fan performance

The variation in airflow velocity in each duct of the fan for different working loads is illustrated in Fig. 17. As shown in Fig. 17(a)–(d), the resistance to airflow rose significantly as the working load increased from $c_f = 0$ to 8.77. The corresponding total airflow flow rates (Q) from three ducts were 1.50, 1.44, 1.53 and 1.39 m³ s⁻¹, respectively. This implied that the airflow flow rate and velocity in each fan outlet decreased when the fan working load (c_f) increased. This is due to the

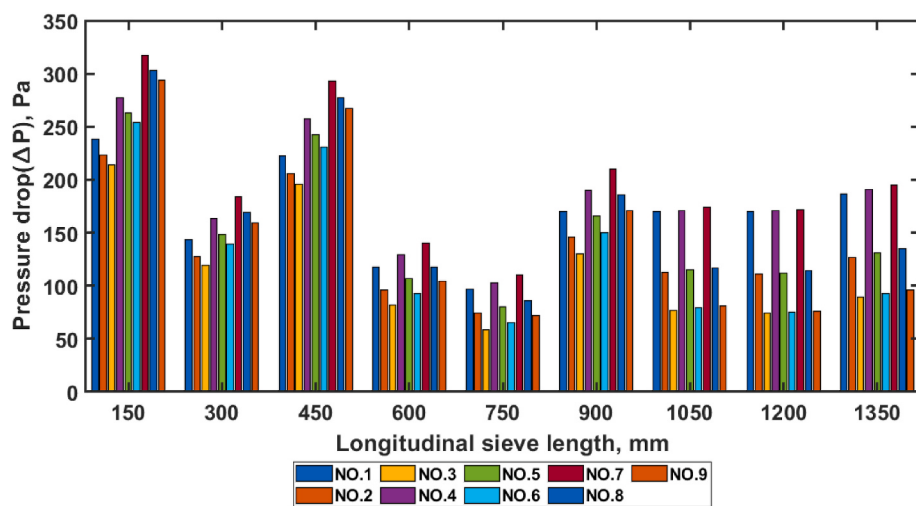


Fig. 14. Total pressure drop (ΔP) along the longitudinal sieve length.

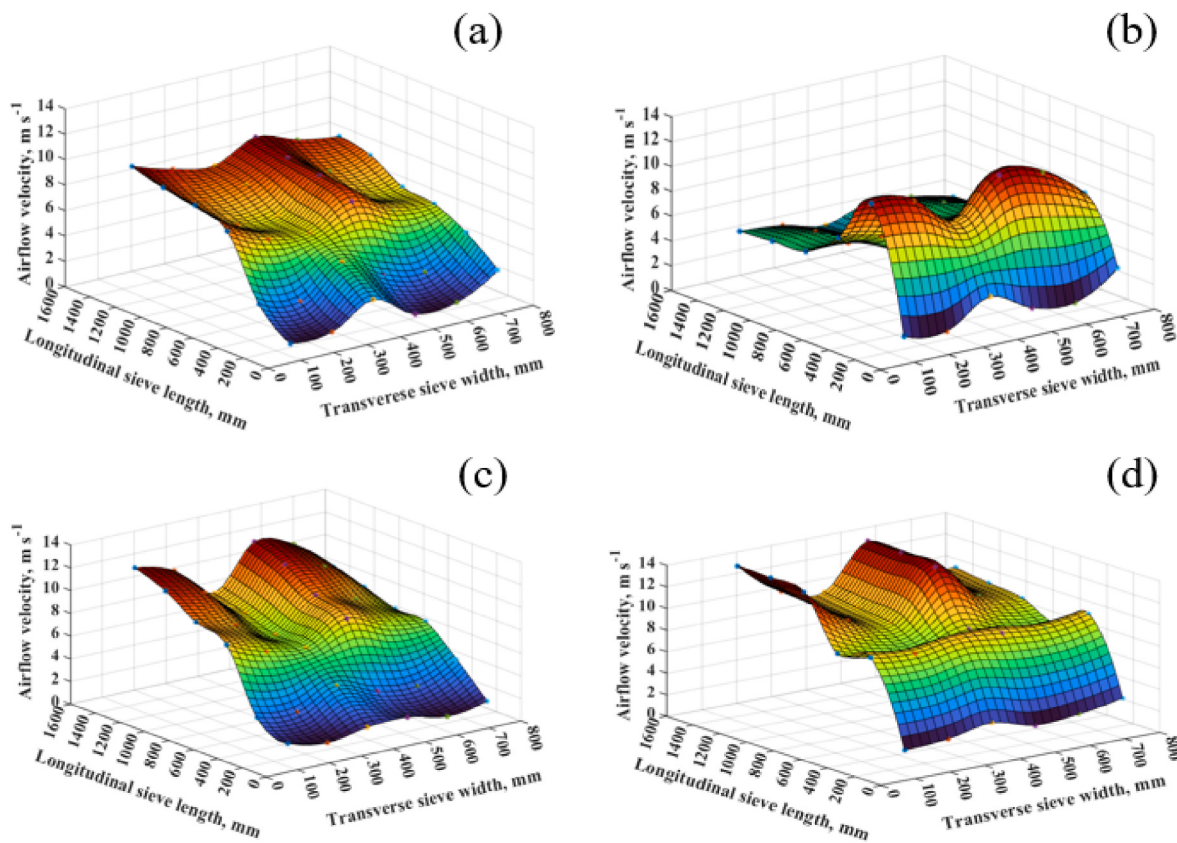


Fig. 15. Airflow velocity below the perforated plates; (a) At $Z = 50$ mm and $R = 1300$ rpm, (b) At $Z = 150$ mm and $R = 300$ rpm, (c) At $Z = 50$ mm and $R = 1500$ rpm, and (d) At $Z = 150$ mm and $R = 1500$ rpm; Z - measurement layer below the perforated plate at Z-axis, and R -fan revolution speed.

fact that higher resistance within the system restricted the airflow movement, leading to reduced airflow rates at the outlet. This reduction in velocity indicated a decrease in the overall efficiency of the fan, as it struggled to push airflow through the sieve and material under higher working load conditions.

Duct III had the largest airflow volume, and this airflow is supposed to be for the tailing sieve. In order to get better grain fluidisation in the front sieve section, the guide plate angle should be adjusted for optimal airflow distribution. Under different working loads the average airflow velocity at Duct I remained larger than the suspension velocity of the

rice grain, which is important for the initial material layer breakdown. In the lower Duct III, the maximum airflow velocity recorded was 10.25–13.5 m s⁻¹, and the aerodynamic pressure created by the fan should be enough for grain fluidisation.

The simulated pressure contour plots for the fan (Fig. 18) show the variations in pressure under different loads. The total pressure inside the fan and within its ducts increased with higher working loads. Increased loads demand greater airflow resistance, leading to enhanced pressure levels throughout the system. As a result, a maximum total pressure was observed at Duct III when the resistance coefficient (c_f) was 0, and it

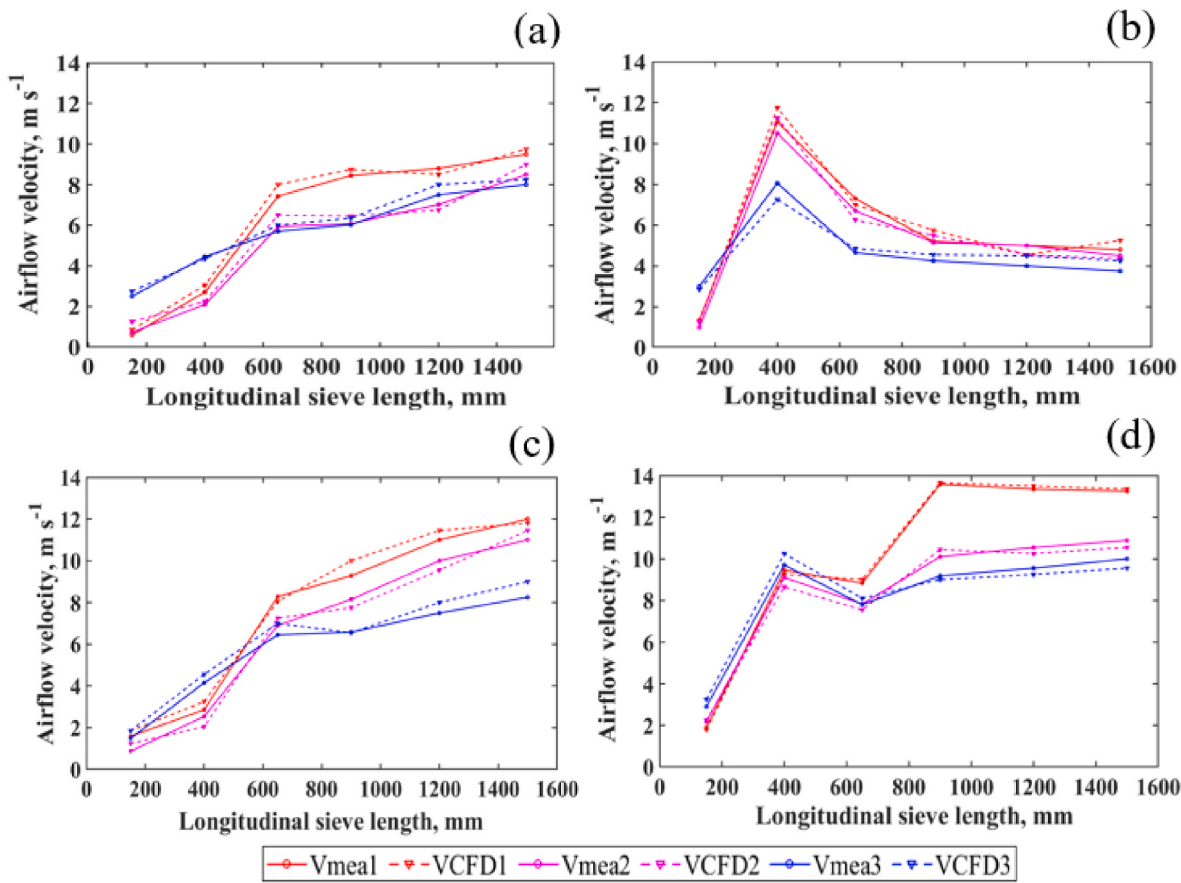


Fig. 16. CFD model validation; (a) At $Z = 50$ mm and $R = 300$ rpm, (b) At $Z = 150$ mm and $R = 1300$ rpm, (c) At $Z = 50$ mm and $R = 1500$ rpm, (d) At $Z = 150$ mm and $R = 1500$ rpm; Vmea - measured airflow velocity at specific point, VCFD - simulated airflow velocity at specific point, Z - measurement layer below the perforated plate at Z-axis, R - fan revolution speed.

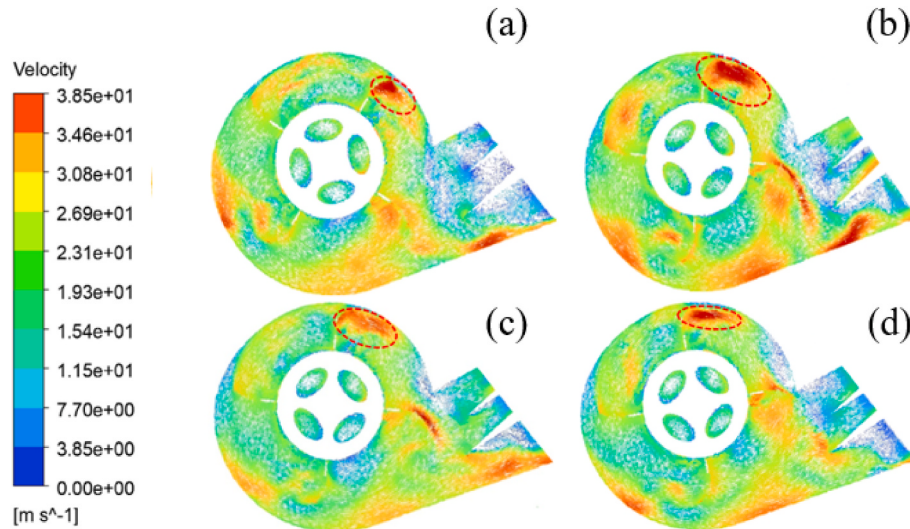


Fig. 17. Airflow velocity of existing fan under various working load, guide plate angle of I and II = 30° , fan speed of 1300 rpm; (a) $c_f = 0$, (b) $c_f = 5.93$, (c) $c_f = 7.28$, and (d) $c_f = 8.77$.

decreased as the resistance increased. The recorded total pressures were 714.51 Pa for $c_f = 0$, 670.32 Pa for $c_f = 5.93$, 581.58 Pa for $c_f = 7.28$, and 506.82 Pa for $c_f = 8.77$. This trend indicated that increasing airflow resistance significantly reduced the total pressure within the cleaning system.

From the fan performance curve shown in Fig. 19(a), it can be seen

that the highest airflow volume rate at Duct I, which supplies airflow to the front sieve, was recorded under test condition 3 (see Table 1), corresponding to a feed rate of 5 kg s^{-1} , a sieve opening of 30 mm, guide plate angles of $I = 30^\circ$ and $II = 28^\circ$, with the corresponding airflow ranging between 0.63 and $0.72 \text{ m}^3 \text{ s}^{-1}$. In contrast, the lowest airflow volume rate, ranging from 0.33 to $0.42 \text{ m}^3 \text{ s}^{-1}$, was observed under test

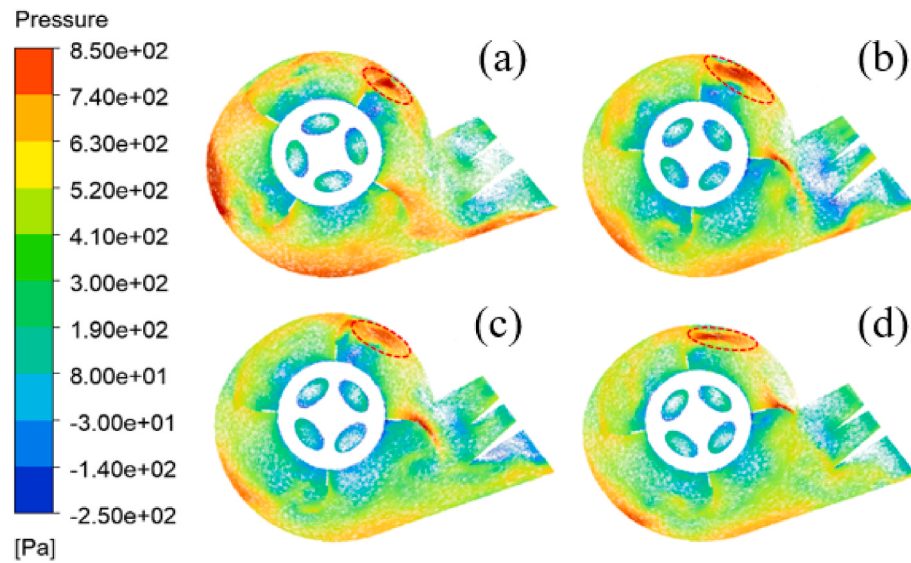


Fig. 18. Total pressure of existing fan under various working load, guide plate angle of I and II = 30°, fan speed of 1300 rpm; (a) $c_f = 0$, (b) $c_f = 5.93$, (c) $c_f = 7.28$, and (d) $c_f = 8.77$.

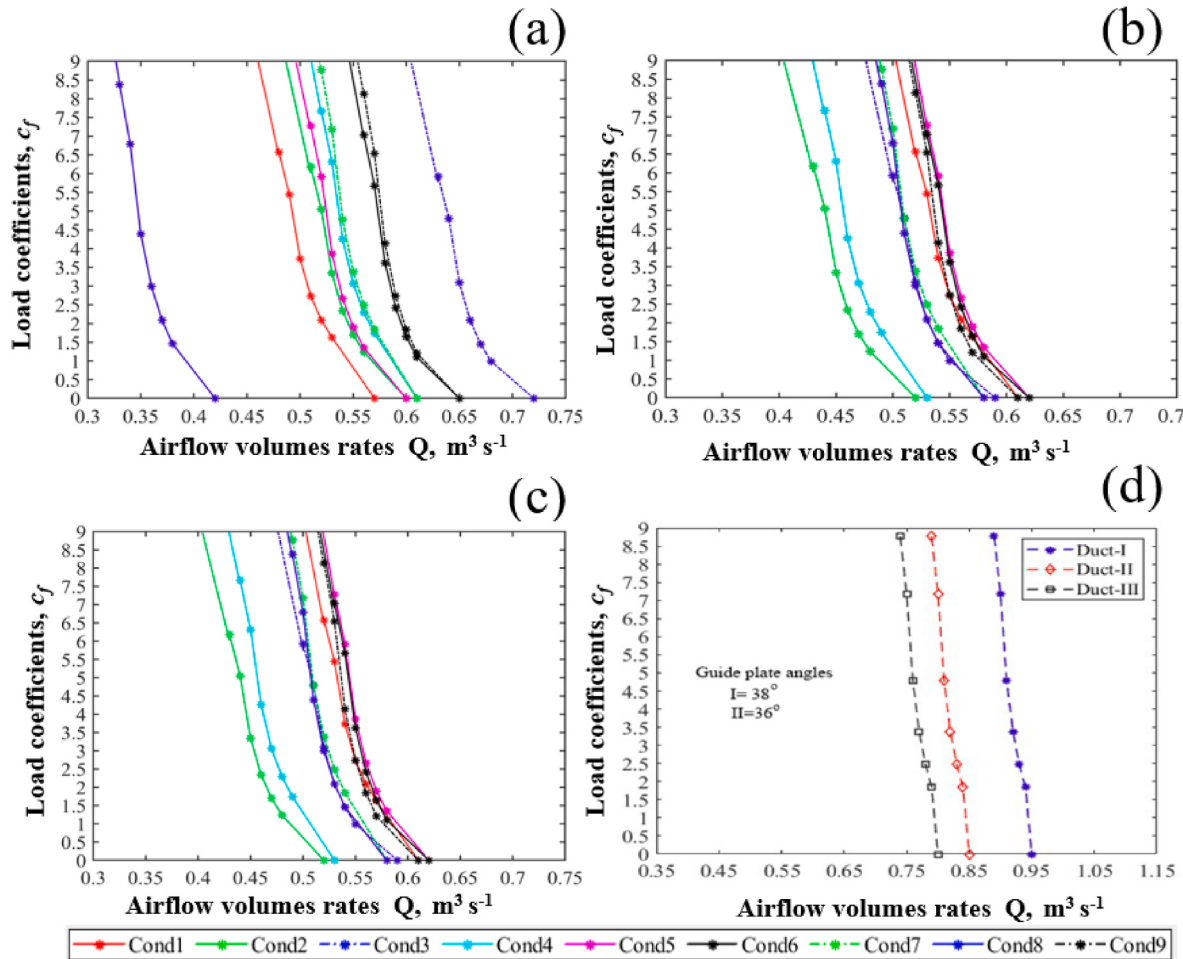


Fig. 19. Fan performance curve ('Cond.' Stands for 'test conditions' refer [Table 1](#)); (a) Duct I, (b) Duct II, (c) Duct III, and (d) Optimised setting.

condition 8, which had a higher feed rate of 7 kg s^{-1} and a smaller sieve opening of 26 mm. These findings suggest that both material accumulation and the sieve opening ratio significantly influenced the airflow volume at the fan outlets. Greater material layers and smaller sieve

openings increased resistance to airflow, thereby reducing the volume delivered through the front duct. This highlighted the importance of considering feed rate and sieve configuration in fan design and airflow management to ensure uniform and efficient cleaning performance.

Field observations revealed that material accumulation was highest at the front sieve, compared to the middle and rear sections. This uneven distribution of threshed material increased airflow resistance in the front region, thus demanding a higher airflow volume to maintain effective separation. In contrast, the airflow volume rate at Duct II, which supplied air to the middle sieve, was relatively uniform across all test conditions, as shown in Fig. 19(b). The airflow ranged from 0.52 to 0.62 $\text{m}^3 \text{s}^{-1}$, with minimal variation despite changes in feed rates and sieve openings. This stability indicated that the middle region of the sieve experienced less material accumulation and more consistent airflow resistance, resulting in a steadier airflow distribution through Duct II. From Fig. 19(c), it can be observed that Duct III exhibited the largest variation in airflow volume under the test condition when the guide plate angles I and II were both set to 38° . It had a high airflow discharge of $1.71 \text{ m}^3 \text{s}^{-1}$, causing the fan to operate at a level that exceeded the recommended airflow for the tailing sieve and leading to high grain loss. In contrast, the optimised working parameter, with guide plate angles of $I = 38^\circ$ and $II = 36^\circ$, the sieve opening 26 mm and fan speed of 1300 rpm, provided an optimal airflow discharge of up to $0.8 \text{ m}^3 \text{s}^{-1}$ at Duct III, which helped to minimise grain loss due to blowing. The corresponding airflow discharge was $0.79, 0.61, 0.78 \text{ m}^3 \text{s}^{-1}$ for Duct I, II and III, respectively and met the recommended airflow for effective grain cleaning. This enhanced airflow facilitated improved grain fluidisation, ensuring that the grains were effectively suspended and separated from MOG. From Fig. 19(d), the ΔP_{tot} versus discharge (Q_v) graph, with the optimised setting of guide plate angle of $I = 38^\circ$ and $II = 36^\circ$, a fan speed of 1300 rpm, and a sieve opening of 26 mm, has a steep slope indicating a positive fan performance under the optimised parameter settings, ensuring effective operation under varying operational conditions when harvesting rice.

On the other hand, the fan achieves maximum airflow volumes of $0.59 \text{ m}^3 \text{s}^{-1}$, $0.61 \text{ m}^3 \text{s}^{-1}$, and $1.54 \text{ m}^3 \text{s}^{-1}$ for Ducts I, II, and III, respectively for guide plate angle of I and $II = 30^\circ$, fan speed of 1300 rpm. This airflow distribution results in lower discharge at the front sieve and higher discharge at the rear sieve. This imbalance in airflow discharge across the sieves adversely impacts the cleaning efficiency, as insufficient airflow in the front sieve area hinders effective separation, while excessive airflow in the rear sieve increases grain loss. However, the optimised fan parameter settings, with guide plate angle of $I = 38^\circ$ and $II = 36^\circ$, a fan speed of 1300 rpm, and a sieve opening of 26 mm, the airflow rates of the optimised fan in Duct I shows an increase of 33.9 %, while Duct II remains unchanged for both settings. However, the airflow discharge for Duct III of the optimised fan is reduced by 49.4 %. This balance can help maintain grain fluidisation and provide sufficient airflow energy for effective grain cleaning. These variations in airflow distribution across the ducts highlight the impact of the optimised fan settings, ensuring improved the airflow velocity at the fan outlet.

3.5. Airflow and pressure distribution analysis for the optimised fan working

The CFD simulations were conducted with the optimised fan parameters under the feed rates of 6 kg s^{-1} , and sieve opening of 26 mm, the corresponding resistance $c_f = 7.28$. The corresponding airflow velocity, total outlet pressure distributions, and internal flow field patterns of the optimised cleaning fan are shown in Fig. 20. From Fig. 20(a), it can be seen that the airflow distribution across each duct was well-balanced, with the share of airflow volume rates at Duct I, II, and III being 36.34 %, 28.03 %, and 35.63 %, respectively. This reasonable distribution ensured efficient airflow management within the system, which was sufficient to fluidise grain mat during the cleaning operation, contributing to improved overall performance of the cleaning fan and maintaining optimal conditions for grain separation.

Fig. 20(b) shows that a total pressure of 507.56, 428.43, and 343.74 Pa was obtained for fan ducts I, II, and III, respectively. The high pressure in Duct I was especially important, as it generated the airflow necessary to reach the front sieve section, initiating the breakdown of the grain mat and fluidisation of the accumulated grain, which helped to distribute grains more evenly and prevent clogging, thereby improving overall cleaning performance. In addition, this combination provided the required airflow pressure to force the airflow through the ducts, especially when Duct I was subjected to higher loads.

To keep most of the grains in a fluidised state in the cleaning shoe, aerodynamic forces created by the fan should be less than the gravitational forces acting on the grains and must exceed the gravitational forces acting on the MOG particles. Additionally, these velocities should decrease from the front to the rear to prevent grains from being blown out. From Fig. 21(a), (b)& (d), it can be seen that the airflow velocity vector across the sieve was not uniform, with some vortices forming beneath the sieve, causing airflow to recirculate under the sieve. This prevented partial airflow from being directed to the sieve surface, resulting in a chaotic airflow distribution within the cleaning shoe and hindering the formation of an ideal airflow pattern above the cleaning sieve. The optimal settings of a sieve opening of 26 mm, along with guide plate angles I of 38° and II of 36° , and a fan speed of 1300 rpm, significantly enhanced the airflow velocity distribution inside the cleaning shoe, as shown in Fig. 21(c). These airflow velocities created a uniform airflow distribution across the sieve, breaking up compacted material layers in the front and efficiently lifting accumulated material off the sieve surface, thus ensures more effective grain separation.

Fig. 22 illustrates the airflow distribution inside the cleaning shoe and beneath the sieve under various parameter settings. Among them, the optimal configuration exhibited the highest airflow velocity both above and below the sieve. Specifically, beneath the sieve, the airflow velocities ranged from 8.50 to 9.0 m s^{-1} at the front section, 5.25 – 5.75 m s^{-1} at the middle section, and 3.25 – 3.75 m s^{-1} at the rear section.

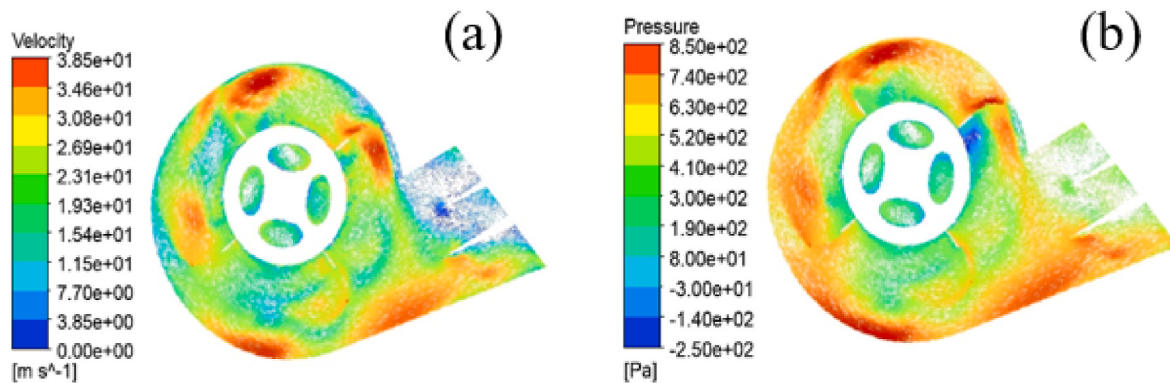


Fig. 20. Airflow velocity and pressure distribution of optimised setting with $c_f = 7.28$ (guide plate angle $I = 38^\circ$ and $II = 36^\circ$, fan speed of 1300 rpm); (a) Airflow velocity, m s^{-1} , and (b) Total pressure, Pa.

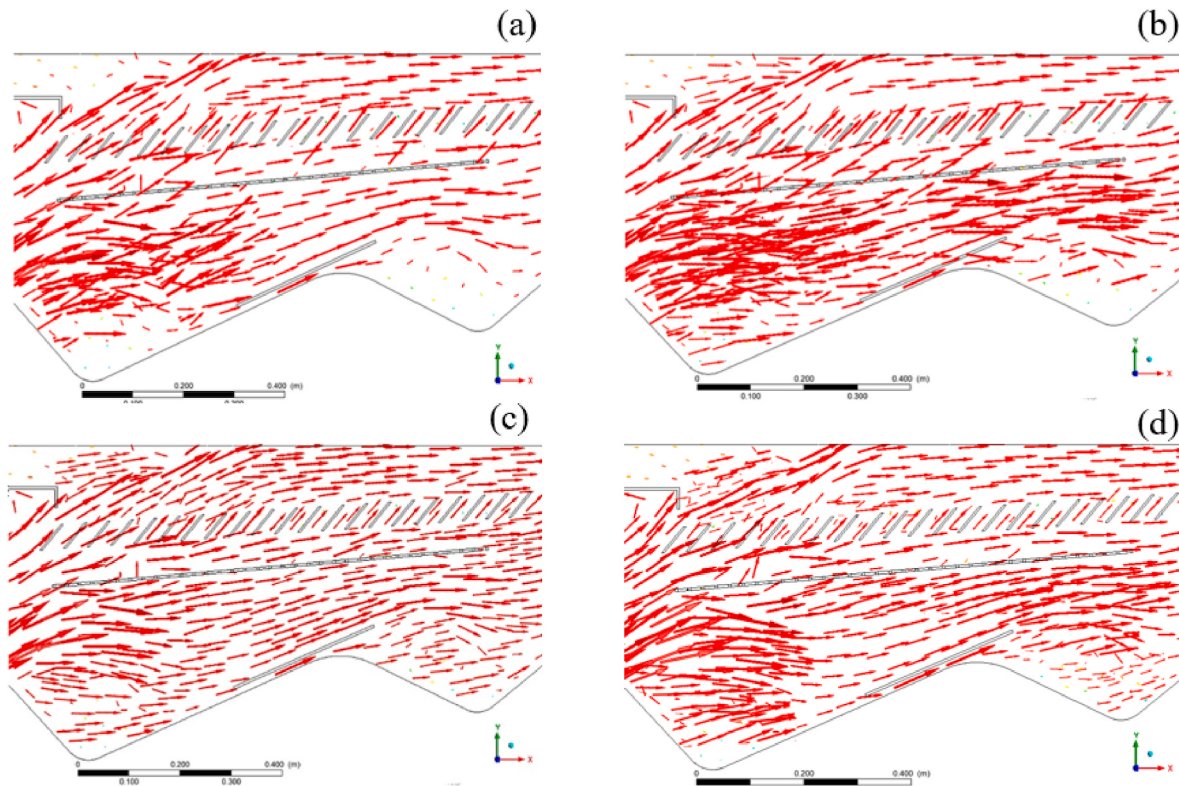


Fig. 21. Airflow velocity and pressure distribution with optimised working parameter, fan revolution speed $R = 1300$ rpm, sieve opening = 26 mm; (a) Guide plate angle I = 30° , II = 28° , (b) Guide plate angle I = 34° , II = 30° , (c) Guide plate angle I = 38° , II = 36° , and (d) Guide plate angle I = 42° , II = 42° .

These airflow conditions generated sufficient force to break up compacted material layers at the front of the sieve and effectively lift accumulated material from the sieve surface. A balanced airflow distribution above the sieve contributed to improved separation efficiency between grain and MOG. This optimisation can contribute to reduced grain losses, lower impurity levels, and improved operational efficiency, offering substantial benefits for modern rice production.

3.6. Field validation with optimised parameter setting

The performance of the cleaning fan under optimised settings was evaluated in terms of grain loss and impurity ratio across different operational parameter combinations in the same field. The results are presented in Table 5 and it can be seen that a sieve opening of 22 mm and fan speeds of 1500 rpm resulted in increased grain loss reaching

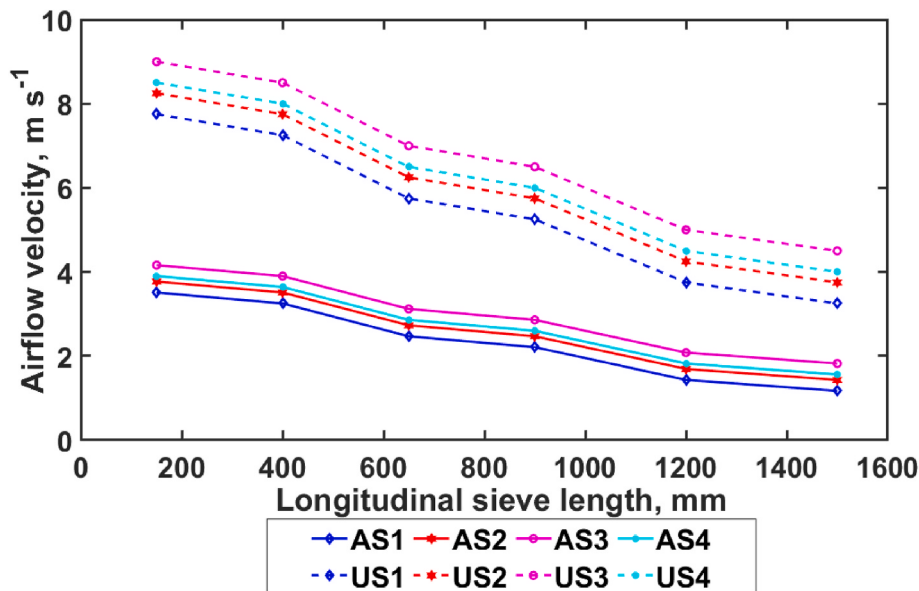


Fig. 22. Airflow velocity distribution along sieve length above and under the sieve; AS1-Airflow velocity above the sieve with guide plate angle I = 30° and II = 28° , AS2 - guide plate angle I = 34° and II = 30° , AS3 - guide plate angle I = 38° and II = 36° , AS4 - guide plate angle I = 42° and II = 42° ; US1-Airflow velocity under the sieve with guide plate angle I = 30° and II = 28° ; US2 - guide plate angle I = 34° and II = 34° ; US3 - guide plate angle I = 38° and II = 36° ; US4 - guide plate angle I = 42° and II = 42° .

1.22 %, which exceeded the standard limit. Under these conditions, heavier material clogged the sieve openings, preventing grain from passing through the chaffer, and resulting in more grain being expelled at the back of the harvester. Higher airflow velocities, needed to fluidise this heavier material, inadvertently lifted and ejected more grain along with the chaff. This finding highlights the impact of excessive fan speeds on cleaning performance and the importance of carefully adjusting fan speed and sieve opening to meet efficiency standards. Additionally, excessive airflow disrupted the grain mat on the sieves, causing more grain to be expelled from the rear of the cleaning shoe. Moreover, the results showed that larger sieve openings correlated with higher impurity ratios. Wider openings allowed more unwanted material, such as chaff and debris, to pass through alongside the grain. For example, at a sieve opening of 30 mm, a fan speed of 1100 rpm, and a guide plate angle I of 30° and II of 28°, the maximum recorded impurity ratio reached 1.65 %. The combination of large sieve openings and low fan speeds enabled more MOG to pass through without sufficient separation. This emphasises the need to optimise fan speed to ensure effective separation and reduce impurity levels. A larger sieve opening combined with low fan speed reduced the separation efficiency, allowing more debris and chaff to mix with the clean grain due to insufficient airflow for proper fluidisation.

From the data presented in Table 5 on the optimised fan settings, it can be confirmed that a sieve opening of 26 mm, guide plate angle I of 38° and II of 36°, and a fan speed of 1300 rpm met the criteria for effective cleaning performance. These settings resulted in a grain sieve loss ratio of 0.78 % and a grain impurity ratio of 1.15 % at a feed rate of 6 kg s⁻¹. This combination achieved a satisfactory balance between reducing grain loss and impurity levels, ensuring high efficiency and quality in the cleaning process. The findings demonstrated that precise adjustments to the guide plate angles can significantly optimise airflow, thereby improving grain mat fluidisation and the overall cleaning performance of combine harvesters.

Future research should focus on innovative fan designs that could improve airflow uniformity and advance the effectiveness of cleaning systems in longitudinal flow rice combine harvesters. Additionally, integrating real-time monitoring technology could enable dynamic adjustments to airflow and material distribution, further enhancing overall cleaning performance.

4. Conclusion

This study aimed to optimise the cleaning performance of a longitudinal-flow rice combine harvester through experimental analysis and CFD simulations. The distribution of threshed output across different sieve zone revealed uneven grain accumulation, particularly in the front and side regions, which increased airflow resistance. CFD simulations further demonstrated that higher fan working loads reduced airflow volume at the fan ducts due to increased system resistance. Both experiments and simulations confirmed that excessive grain accumulation significantly elevated airflow resistance and that the fan's working load strongly influenced airflow distribution. Optimisation of fan parameters using a DOE approach identified an optimal configuration consisting of a 26 mm sieve opening, guide plate angles of 38° (I) and 36° (II), and a fan speed of 1300 rpm. This setup notably improved airflow distribution. Field experiments validated the optimisation, achieving a sieve loss ratio of 0.78 % and an impurity ratio of 1.15 % at a feed rate of 6 kg s⁻¹. The optimised fan settings enhanced cleaning efficiency and reduced grain loss, thereby improving overall combine harvester performance and farmer profitability. These findings provide a systematic basis for determining fan working loads and optimising operating parameters, while also offering valuable insights for future structural optimisation of cleaning fans in rice combine harvesters.

Table 5
Field experiment result with optimised parameter settings.

| Test No. | Fan Speed (rpm) | Guide plate angle I (°) | Guide plate angle II (°) | Sieve Opening (mm) | Grain loss (%) | Grain Impurity ratio (%) |
|----------|-----------------|-------------------------|--------------------------|--------------------|----------------|--------------------------|
| 1 | 1100 | 30 | 28 | 22 | 0.85 | 1.30 |
| 2 | 1100 | 34 | 30 | 26 | 0.82 | 1.45 |
| 3 | 1100 | 30 | 28 | 30 | 0.92 | 1.65 |
| 4 | 1300 | 38 | 36 | 26 | 0.78 | 1.15 |
| 5 | 1300 | 34 | 30 | 22 | 0.81 | 1.17 |
| 6 | 1300 | 38 | 36 | 30 | 0.89 | 1.23 |
| 7 | 1500 | 30 | 28 | 26 | 1.15 | 1.08 |
| 8 | 1500 | 34 | 30 | 30 | 1.05 | 1.10 |
| 9 | 1500 | 38 | 36 | 22 | 1.22 | 0.95 |

CRediT authorship contribution statement

Zhenwei Liang: Writing – review & editing, Supervision. Million Eyasu Wada: Writing – original draft, Validation, Software, Methodology, Investigation, Formal analysis, Data curation.

Declaration of competing interest

The authors declare that they have no known competing financial interests or personal relationships that could have appeared to influence the work reported in this paper.

Acknowledgement

This research was funded by the National Natural Science Foundation of China (52275251); Sponsored by QingLan Project of Jiangsu Province, China; The Young Talents Cultivation Program of Jiangsu University, China (2022); Agricultural science and Technology Support Program of Taizhou, China (TN202208); A Project Funded by Priority Academic Program Development of Jiangsu Higher Education Institutions (NO.PAPD-2023-87).

Data availability

The datasets generated during and/or analysed during the current study are available from the corresponding author upon reasonable request.

References

- Brooker, D. B., Bakker-Arkema, F. N., & Hall, C. W. (1992). *Drying and storage of grains and oilseeds*. New York: AVI Publication.
- Chen, M., Chen, Z., Gong, M., Tang, Y., & Liu, M. (2021). CFD-DEM-VDGM method for simulation of particle fluidisation behavior in multi-ring inclined-hole spouted fluidised bed. *Particuology*, 57(4), 112–126. <https://doi.org/10.1016/j.partic.2021.01.004>
- Chu, S. L. (2014). Experimental research on the axial-flow impeller aerodynamic performance of the axial-flow fan. *Fluid Machinery*, 42(4), 6–10. <https://doi.org/10.3969/j.issn.1005-0329.04.002>
- Collar, A. R. (1939). The effect of a gauze on the velocity distribution in a uniform duct, British aeronautical research council. *Reports and Memoranda No.1867*.
- Ding, B. C., Liang, Z. W., Qi, Y., Ye, Z., & Zhou, J. (2022). Improving cleaning performance of rice combine harvesters by DEM-CFD coupling technology. *Agriculture*, 12(9), 1457. <https://doi.org/10.3390/agriculture12091457>
- FLUENT, Inc. (2006). *FLUENT 6.3 User's guide*. Lebanon, NH.
- Gebrehiwot, M. G., De Baerdemaeker, J., & Baelmans, M. (2010a). Effect of a cross-flow opening on the performance of a centrifugal fan in a combine harvester. *Biosystems Engineering*, 105, 247–256. <https://doi.org/10.1016/j.biosystemseng.2009.11.003>
- Gebrehiwot, M. G., De Baerdemaeker, J., & Baelmans, M. (2010b). Numerical and experimental study of a cross flow fan for combine cleaning shoes. *Biosystems Engineering*, 106(4), 448–457. <https://doi.org/10.1016/j.biosystemseng.2010.05.009>
- Hall, C. (1980). *Drying and storage of crops*. Westport, CN: AVI Publication. <https://doi.org/10.1002/food.19820260613>
- Idelchik, I. E. (2008). *Handbook of hydraulic resistance* (4th ed.). Moscow, Russia: Research Institute of Gas Purification.

- Ji, K. Z., Li, Y. M., Liang, Z. W., Liu, Y. B., Cheng, J. H., Wang, H. H., Zhu, R. H., Xia, S. B., & Zheng, G. Q. (2022). Device and method suitable for matching and adjusting reel speed and forward speed of multi-crop harvesting. *Agriculture-Basel*, 12(2), 213. <https://doi.org/10.3390/agriculture12020213>
- Ji, L. L., Li, W., Shi, W. D., Shao, P. P., & Jiang, X. P. (2017). Influence of different blade numbers on unsteady pressure pulsations of internal flow field in mixed-flow pump. *Journal of Drainage and Irrigation Machinery Engineering*, 35(8), 666–673. <https://doi.org/10.3969/j.issn.1674-8530.16.0042>, 699.
- Kenney, K. L., Wright, C. T., & Bryden, K. M. (2005). Virtual engineering approach to developing selective harvest technologies. *Transactions of the ASABE*, 7, 5427–5437. <https://doi.org/10.13031/2013.19561>
- Korn, C., Hübner, R., Herlitzius, T., Rüdiger, F., & Fröhlich, J. (2013). Numerical study of airflow in a combine cleaning shoe. *Die Landtechnik*, 68(2), 83–88.
- Li, F., & Li, Y. (2015). Optimisation and simulation research of the airway of tangential-axial combine harvester cleaning room. *Journal of Agricultural Mechanisation Research*, 2, 75–78. <https://doi.org/10.13427/j.cnki.njyi.2015.02.018>
- Li, Y., Xu, L. Z., Zhou, Y., Li, B., Liang, Z. W., & Li, Y. M. (2018). Effects of throughput and operating parameters on cleaning performance in air-and-screen cleaning unit. *Computers and Electronics in Agriculture*, 152(5), 141–148. <https://doi.org/10.1155/2020/4121595>
- Liang, Z. W., Li, Y. M., De Baerdemaeker, J., Xu, L. Z., & Saeyns, W. (2019). Development and testing of a multi-duct cleaning device for tangential-longitudinal flow rice combine harvesters. *Biosystems Engineering*, 182, 95–106. <https://doi.org/10.1016/j.biosystemseng.2019.04.004>
- Liang, Z. W., Li, Y., Xu, L., & Zhao, Z. (2016). Sensor for monitoring rice grain sieve losses in combine harvesters. *Biosystems Engineering*, 147, 51–66. <https://doi.org/10.1016/j.biosystemseng.2016.03.008>
- Liang, Z. W., & Million, E. W. (2023). Development of cleaning systems for combine harvesters: A review. *Biosystems Engineering*, 236, 79–102. <https://doi.org/10.1016/j.biosystemseng.2023.10.018>
- Liang, Y. Q., Tang, Z., Zhang, H., & Li, Y. (2022). Cross-flow fan on multi-dimensional airflow field of air screen cleaning system for rice grain. *International Journal of Agricultural and Biological Engineering*, 15(4), 223–235. <https://doi.org/10.25165/j.ijabe.20221504.6949>.
- Liang, Z. W., Xu, L. Z., De Baerdemaeker, J., Li, Y. M., & Saeyns, W. (2020). Optimisation of a multi-duct cleaning system for rice combine harvesters utilising CFD and experiments. *Biosystems Engineering*, 190, 25–40. <https://doi.org/10.1016/j.biosystemseng.2019.11.016>
- Liu, Y. B., Li, Y. M., Ji, K. Z., Yu, Z. W., Ma, Z., Xu, L. Z., & Niu, C. H. (2025). Development of a hydraulic variable-diameter threshing drum control system for combine harvester, part I: Adaptive monitoring method. *Biosystems Engineering*, 250, 174–182. <https://doi.org/10.1016/j.biosystemseng.2025.01.001>
- Liu, Y. B., Li, Y. M., Zhang, T., & Huang, M. S. (2022). Effect of concentric and non-concentric threshing gaps on damage of rice straw during threshing for combine harvester. *Biosystems Engineering*, 219, 1–10. <https://doi.org/10.1016/j.biosystemseng.2022.04.013>
- Liu, Z., Zheng, Y., Wang, Z., Chen, D., & Wang, J. (2015). Design on air-flowing cleaning unit of micro rice-wheat combine harvester. *Transactions of the Chinese Society for Agricultural Machinery*, 46(7), 102–108 (In Chinese) <https://doi.org/10.6041/j.issn.1000-1298.2015.07.016>.
- Ma, Z., Zhang, Z. L., Zhang, Z. H., Song, Z. Q., Liu, Y. B., Li, Y. M., & Xu, L. Z. (2023a). Durable testing and analysis of a cleaning sieve based on vibration and strain signals. *Agriculture*, 13, 2232. <https://doi.org/10.3390/agriculture13122232>
- Ma, Z., Zhu, Y. L., Li, J. L., Song, Z. Q., Yu, J., Li, Y. M., & Xu, L. Z. (2024). Study on the performance of detection air duct and evaluation index of agricultural cleaning centrifugal fans. *Biosystems Engineering*, 239, 81–97. <https://doi.org/10.1016/j.biosystemseng.2024.01.015>
- Ma, Z., Zhu, Y. L., Wu, Z. P., Traore, S. N., Chen, D., & Xing, L. C. (2023b). BP neural network model for material distribution prediction based on variable amplitude anti-blocking screening DEM simulations. *International Journal of Agricultural and Biological Engineering*, 16, 190–199. <https://doi.org/10.25165/j.ijabe.20231604.7178>
- Nie, L., & Peng, S. (2017). *Rice production worldwide (chapter two: Rice production in China)*. Springer International Publishing. <https://doi.org/10.1007/978-3-319-47516-52>
- Peng, S. B., Tang, Q. Y., & Zou, Y. B. (2009). Current status and challenge of rice production in China. *Plant Production Science*, 12(1), 3–8. <https://doi.org/10.1626/ppls.12.3>
- Qing, Y. R., Li, Y. M., Xu, L. Z., Ma, Z., Tan, X. L., & Wang, Z. (2021b). Oilseed rape (*Brassica napus L.*) pod shatter resistance and its relationship with whole plant and pod characteristics. *Industrial Crops and Products*, 166, Article 113459. <https://doi.org/10.1016/j.indcrop.2021.113459>
- Qing, Y. R., Li, Y. M., Yang, Y., Xu, L. Z., & Ma, Z. (2021a). Development and experiments on reel with improved time trajectory for harvesting oilseed rape. *Biosystems Engineering*, 206, 19–31. <https://doi.org/10.1016/j.biosystemseng.2021.02.016>
- Qiu, G. Y. (2006). *Electrical circuit* (5th ed.). Beijing, China: Higher Education Press.
- Seo, S. J., Kim, K. Y., & Kang, S. H. (2003). Calculations of three-dimensional viscous flow in a multi-blade centrifugal fan by modeling blade forces. *Proceedings of The Institution of Mechanical Engineers, Part A. Journal of Power and Energy*, 217, 287–297. <https://doi.org/10.1243/09576500322066510>
- Tabatabaifar, A. (1992). *Airflow and particle motion on an adjustable chaffier sieve (PhD thesis)*. Stadtkolich, USA: Pennsylvania State University-University Park.
- Tabatabaifar, A., & Persson, S. P. E. (1995). Layer breakup and particle movement on a chaffier sieve. *Transactions of the ASAE*, 38(5), 1305–1313. <https://doi.org/10.13031/2013.27952>
- Wang, F. Z., Liu, Y. B., & Ji, K. Z. (2023). Research and experiment on variable-diameter threshing drum with movable radial plates for combine harvester. *Agriculture-Basel*, 13(8), 1487. <https://doi.org/10.3390/agriculture13081487>
- Xu, L. Z., Alan, C. H., Li, Y. M., Liang, Z. W., & Yu, L. J. (2015). Numerical and experimental analysis of airflow in a multi-duct cleaning system for a rice combine harvester. *Transactions of the ASABE*, 59(5), 1101–1110. <https://doi.org/10.13031/trans.59.11569>
- Xu, T., & Li, Y. (2020). Effect of airflow field in the tangential-longitudinal flow threshing and cleaning system on harvesting performance. *Advances in Materials Science and Engineering*, 10, 1–11. <https://doi.org/10.1155/2020/4121595>
- Xu, L. Z., Li, Y. M., Tang, Z., Wang, L. G., & Jiao, Z. Y. (2013). Tangential-longitudinal axial combine harvester. *Transactions of the CSAM*, 44(8), 94–98. <https://doi.org/10.6041/j.issn.1000-1298.2013.08.017>
- Yu, L. J. (2015). *Design and experimental study in cleaning device with double outlet and multi-duct*. MS thesis. Zhenjiang, China: Jiangsu University.
- Yu, Z. W., Li, Y. M., Du, X. X., & Liu, Y. B. (2024). Threshing cylinder unbalance detection using a signal extraction method based on parameter-adaptive variational mode decomposition. *Biosystems Engineering*, 244, 26–41. <https://doi.org/10.1016/j.biosystemseng.2024.05.010>
- Yuan, L. P. (2017). Progress in super-hybrid rice breeding. *Crop Journal*, 5, 100–102. <https://doi.org/10.1016/j.cj.2017.02.001>
- Zhang, T., Li, Y. M., & You, G. L. (2023). Experimental study on the cleaning performance of hot air flow cleaning device. *Agriculture*, 13, 1828. <https://doi.org/10.3390/agriculture13091828>
- Zhao, J. W., & Wu, S. Y. (1989). Research on basic characteristics of grain fluidised bed. *Transactions of the Chinese Society for Agricultural Machinery*, 6(2), 16–24 (In Chinese).